Chapter 10
Coherent Optical Communication Systems

Ioannis Roudas

Abstract The rapid evolution of long-haul optical communications systems, witnessed in the last five years, is due to the gradual adoption of spectrally efficient, multilevel modulation formats, in conjunction with polarization division multiplexing (PDM) and coherent intradyne detection assisted by digital signal processing (DSP). The objective of this tutorial chapter is to briefly review the operating principles of state-of-the-art long-haul coherent optical communications systems. Due to limitations in space, it focuses mainly on coherent optical systems using quadrature phase-shift keying (QPSK) modulation.

10.1 Introduction

The commercialization in 2008 of the first 40 Gb/s coherent optical communications systems employing polarization division multiplexing (PDM) Quadrature phase-shift keying (QPSK) and intradyne detection assisted by digital signal processing (DSP) marked a major milestone in long-haul transmission [1, 2].

Coherent receivers were intensively studied in the eighties [3–7] because of their superiority to their direct-detection counterparts, mainly in terms of sensitivity and frequency selectivity. However, they were considered impractical at the time, due to their high cost and complexity, as well as their vulnerability to phase-noise and polarization rotations. The revived interest in coherent detection is largely due to the substitution of previously proposed analog electronic and

I. Roudas (✉)
Department of Electrical Engineering
University of Patras
26504 Rio, Greece
e-mail: roudas@ece.upatras.gr

optoelectronic modules (which were bulky, slow, expensive, and largely inefficient) in coherent optical receivers with relatively inexpensive, high-speed, application-specific integrated circuits (ASICs) (see recent surveys [8–11, 15] and the references therein). The latter enable adaptive electronic equalization of linear transmission impairments, i.e., chromatic dispersion, polarization mode dispersion and polarization-dependent loss, and to some extent, of fiber nonlinearities. They also allow for adaptive electronic compensation of imperfections of the analog optical transmitter and receiver front-ends, such as time skew of quadrature components and polarization tributaries, quadrature and polarization imbalance, etc. Finally, they perform all standard digital receiver functionalities such as digital clock recovery, intermediate frequency offset and phase-noise estimation, symbol decision, differential decoding, forward error correction, etc.

There is an emerging consensus among major system vendors that coherent optical PDM-QPSK communications systems are the most attractive candidates for 100 Gb/s Ethernet[1] transmission over existing terrestrial networks [2, 12, 16–19].

At the moment, several companies have announced the development of application-specific integrated circuits (ASICs) for DSP in coherent homodyne synchronous PDM-QPSK receivers operating at this symbol rate. Furthermore, recent field trials [21, 22] have demonstrated the practicality of long-haul 28 GBd coherent optical PDM-QPSK systems.

PDM M-ary Quadrature Amplitude Modulation (M-QAM) is actively investigated for use in next-generation long-haul terrestrial optical communications systems [12]. This modulation format is intended for either single carrier or multi-carrier systems using orthogonal frequency division multiplexing (OFDM), in order to achieve equivalent bit rates of the order of 400 Gb/s or even 1 Tb/s per wavelength channel [12]. PDM M-QAM allows for a nominal spectral efficiency of 2 M b/s/Hz. Recent hero experiments using coherent optical PDM M-QAM communication systems achieved several world records, most notably unprecedented aggregate WDM bit rates approaching 70 Tb/s [23, 24] and a spectral efficiency close to 12 b/s/ Hz [25].

Due to the proliferation of research studies on coherent optical PDM-QPSK and PDM M-QAM communication systems during the last five years, it is difficult to exhaustively cover all aspects of this topic here. The objective of this tutorial chapter is to briefly review the operating principles in long-haul PDM-QPSK coherent optical communications systems.

---

[1] Actually, it is necessary to use an effective bit rate of 112 Gb/s, which corresponds to a symbol rate of PDM-QPSK of 28 GBd, in order to achieve a net per channel 100 Gb/s data rate transmission. The reason is that one must take into account the overhead due to current forward error correction (FEC) ($\sim$7%) and the Ethernet packet header ($\sim$4%). We assume a WDM channel spacing of 50 GHz, which is compatible with the current ITU grid specifications and provides some margin for bandwidth narrowing due to the concatenation of several reconfigurable optical add-drop multiplexers (ROADMs). Then, the spectral efficiency of these systems is 2 b/s/Hz, i.e., half of the nominal spectral efficiency of PDM-QPSK [12–14].

The rest of the chapter is organized as follows: In Sect. 10.2, we initially present the digital M-PSK transmitter and receiver optimal architectures in a block diagram form. Next, we review the operating principle of coherent detection and describe different variants of coherent receivers. In Sect. 10.3, we describe the implementation of the functionalities of the optimal M-PSK transmitter and receiver using various photonic devices, i.e., a QM, a balanced receiver, a phase-diversity receiver with 90° hybrid, and a polarization-diversity receiver. In Sect. 10.4, we review the most prominent DSP algorithms. Finally, in Sect. 10.5, we develop an abstract model for the performance evaluation of an optical communication system using M-PSK modulation and synchronous homodyne detection. The details of the calculations are given in the Appendices.

10.2 Multilevel Differential Phase-Shift Keying

Multilevel phase-shift keying (M-PSK) is a type of digital modulation format whereby information is encoded into discrete changes $\Delta\phi_k$ of the phase of the carrier at time instants equal to multiples of the symbol period [26, 29]. Since phase changes are less affected by additive white Gaussian noise compared to amplitude changes, this modulation format exhibits higher sensitivity than amplitude shift keying (ASK).

10.2.1 Signal Representation

The M-PSK signal can be written as [26]

$$s(t) = \Re\{\tilde{s}(t)e^{j\omega_s t}\} \tag{10.1}$$

where $\Re\{.\}$ denotes the real part and $\tilde{s}(t)$ is the complex envelope

$$\tilde{s}(t) = A\sum_{k=0}^{N-1} c_k g(t - kT) \tag{10.2}$$

where A is the carrier amplitude, N is the number of transmission symbols, T is the symbol period, $g(t)$ is the symbol shape, and we defined the complex symbols

$$c_k \equiv e^{j\Delta\varphi_k} \tag{10.3}$$

In Eq. 10.3, the discrete phase changes $\Delta\phi_k$ take values in the set

$$\{2\pi(i-1)/M + \Phi\}_{i=1}^{M} \tag{10.4}$$

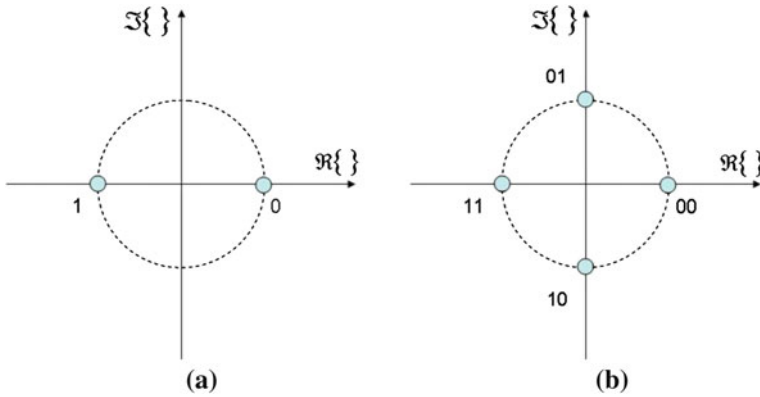where Φ is an arbitrary initial phase.

Fig. 10.1 Geometrical representation of M-PSK signal sets on the complex plane
a $M = 2, \Phi = 0$; **b** $M = 4, \Phi = 0$

Substituting Eqs. 10.2, 10.3 into Eq. 10.1 and using trigonometric identities, we can express M-PSK modulation as the superposition of two carriers at the same frequency but with 90° phase difference carrying M-ary amplitude modulations (called *in-phase* and *quadrature components*)

$$s(t) = \underbrace{I(t) \cos \omega_s t}_{\substack{\text{in−phase} \\ \text{component}}} - \underbrace{Q(t) \sin \omega_s t}_{\substack{\text{quadrature} \\ \text{component}}} \qquad (10.5)$$

where

$$I(t) = A \sum_{k=0}^{N-1} \cos \Delta\phi_k g(t - kT)$$
$$Q(t) = A \sum_{k=0}^{N-1} \sin \Delta\phi_k g(t - kT) \qquad (10.6)$$

From Eqs. 10.3, 10.4, we observe that symbols c_k can take M discrete complex values. A geometric representation of this set of M complex values is shown in Fig. 10.1. The symbols are represented on the complex plane as a constellation of equidistant points on a circle.

It is worth noting that random bits at the entrance of the transmitter must be mapped into the M discrete complex values that symbols c_k can take prior to transmission. In Fig. 10.1, words of $m = \log_2 M$ bits are associated with different constellation points using Gray coding, e.g., words corresponding to adjacent constellation points differ by a single bit (see details below).
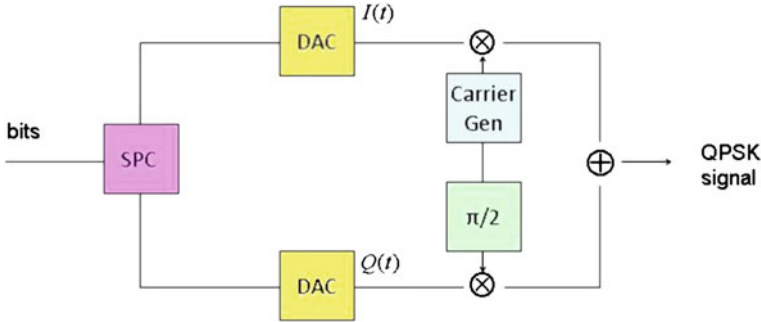
Fig. 10.2 QPSK transmitter (Symbols: SPC: Serial-to-parallel converter, DAC: Digital-to-analog converter, Carrier gen: Carrier generator, $\pi/2$: 90 deg. Phase shifter)

10.2.2 Transmitter and Receiver Architectures

From Eqs. 10.5, 10.6 it is straightforward to derive the block diagram of the QPSK transmitter. Figure 10.2 shows an example of implementation of an ideal QPSK transmitter for $\Phi = \pi/4$. The transmitter does not segment the input PRBS into words of two bits but instead, uses a serial-to-parallel converter to alternatively send bits to two binary pattern generators. These produce two baseband antipodal binary waveforms with instantaneous amplitude $\pm 1/\sqrt{2}$ at symbol rate $R = 1/T$, which modulate two CW carriers $A \cos \omega_s t$, $-A \sin \omega_s t$. Therefore, a signaling rate reduction by one-half is achieved. The two quadrature components are added and transmitted in the channel.

The optimal synchronous QPSK receiver structure is shown in Fig. 10.3. A synchronous receiver is equipped with a carrier phase recovery circuit, which computes the carrier phase change θ acquired during propagation. The received waveform is divided into two parts, each multiplied with $\cos(\omega_s t + \theta)$, $-\sin(\omega_s t + \theta)$, respectively, and filtered using two LPFs with impulse response $g(T - t)$ (matched filters). For ideal NRZ pulses, these LPFs can be ideally implemented as integrate and dump (I&D) filters (e.g., finite time integrators which perform a running average of duration T). In the absence of distortion, the waveforms at the output of the I&D filters are smoothed replicas of the baseband amplitude modulating waveforms $I(t), Q(t)$. These signals are sampled once per symbol, at the appropriate sampling instants, which are calculated using a symbol synchronization circuit, in order to minimize the error probability. Two binary decision devices, with thresholds equal to zero, are used to recover the bits. The decisions are made independently in the two receiver branches. Finally, the recovered binary sequences are combined into a single bit stream using a parallel-to-serial converter.
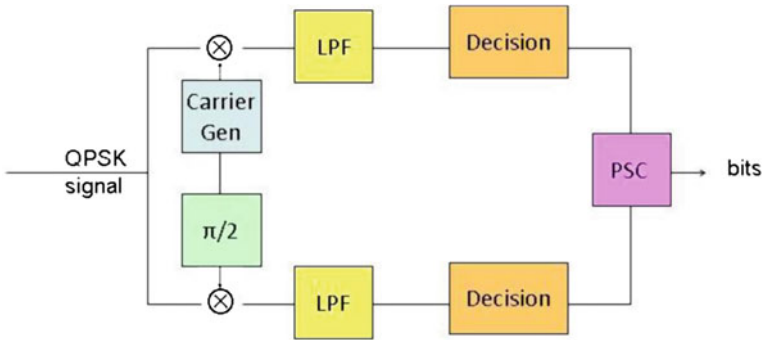
Fig. 10.3 Optimal synchronous QPSK receiver. (Symbols: Carrier gen: Carrier generator, π/2: 90 deg. Phase shifter, LPF: Lowpass filter, Decision: decision circuit, SPC: Serial-to-parallel converter)
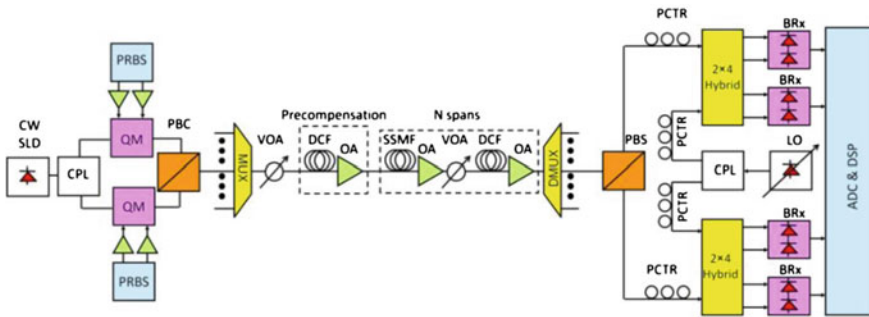

Fig. 10.4 Block diagram of a representative coherent optical PDM-QPSK system. (Symbols: PRBS: Pseudo-random bit sequence, SLD: Semiconductor laser diode, CPL: 3-dB coupler, QM: Quadrature modulator, PBC: Polarization beam combiner, MUX: Optical multiplexer, VOA: Variable optical attenuator, DCF: Dispersion compensating fiber, SSMF: Standard single-mode fiber, OA: Optical amplifier, DMUX: Optical demultiplexer, PBS: Polarization beam splitter, PCTR: Polarization controller, LO: Local oscillator, BRx: Balanced receivers, ADC: Analog-to-digital converter, DSP: Digital signal processing module)

10.2.3 Coherent Optical PDM QPSK System

The implementation of the aforementioned M-PSK transmitter and receiver structures for optical communications, in the case of PDM, is shown in Fig. 10.4.

More specifically, Fig. 10.4 shows the block diagram of a representative long-haul, PDM QPSK optical communications system with a polarization- and phase-diversity coherent optical receiver. At the transmitter, the optical signal from a CW semiconductor laser diode (SLD) is equally split and fed into two parallel quadrature modulators (QM). Two independent maximal-length pseudo-random

bit sequences (PRBS) of period $2^n - 1$, at a bit rate R_b each, drive two QM. The two optical QPSK signals are superimposed with orthogonal SOPs, using a polarization beam combiner (PBC), to form a PDM-QPSK signal. The latter is wavelength division multiplexed (WDM) with additional channels carrying PDM-QPSK signal, using an optical multiplexer (MUX), and transmitted through N amplified spans composed of standard single-mode fiber (SSMF) and, possibly, dispersion compensating fiber (DCF). An additional dispersion pre-compensation module, composed of a DCF and a booster optical amplifier, might be included in the latter case.

The optical receiver front-end is composed of an optical demultiplexer (DMUX), acting as an optical bandpass filter (BPF), a polarization beam splitter (PBS), a laser diode, acting as a local oscillator (LO), two 2×4 90° optical hybrids, and four balanced photodetectors (BRx's). The x- and y-polarization components of the received optical signal and the local oscillator are separately combined and detected by two identical phase-diversity receivers composed of a 2×4 90° optical hybrid and two BRx's each, at the upper and lower polarization branches, respectively. The photocurrents at the output of the four balanced detectors are low-pass filtered (LPF), sampled at integer multiples of a fraction of the symbol period T_s, using an analog-to-digital converter (ADC), and fed to an application-specific integrated circuit (ASIC) for DSP (see below for details).

The aforementioned components of the M-PSK transmitter and receiver are explained in detail in the next section.

10.3 Optical Components

In this section, we describe the implementation of the functionalities of the optical M-PSK transmitter and receiver using various photonic devices, i.e., a QM, a balanced receiver, a phase-diversity receiver with 90° hybrid, and a polarization-diversity receiver.

10.3.1 Optical Transmitter: Quadrature Modulator

The QM is shown in Fig. 10.5 [28]. It is composed of a Mach–Zehnder interferometer which contains two push–pull Mach–Zehnder modulators [43], one in each arm, and a phase modulator at the lower arm that introduces a phase difference between the two arms.

The complex envelope of the modulated electric field at the output of the modulator $\tilde{E}_s(t)$can be written as a function of the unmodulated input electric field $\tilde{E}_{in}(t)$ (see Appendix A)

Fig. 10.5 Quadrature
modulator
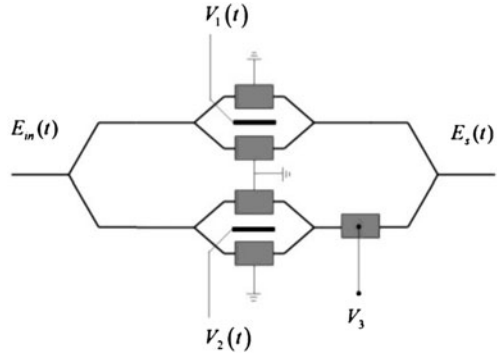
$$\tilde{E}_s(t) = \frac{j}{2} e^{-j\frac{\pi V_3}{2V_{\pi_3}}} \left\{ \sin\left[\frac{\pi V_1(t)}{2V_{\pi_1}}\right] - e^{-j\frac{\pi V_3}{2V_{\pi_3}}} \sin\left[\frac{\pi V_2(t)}{2V_{\pi_2}}\right] \right\} \tilde{E}_{in}(t) \qquad (10.7)$$

where $V_1(t), V_2(t), V_3$ are the driving voltages and $V_{\pi_1}, V_{\pi_2}, V_{\pi_3}$ are the half-wave
voltages of the two Mach–Zehnder modulators and the phase shifter, respectively.

The two Mach–Zehnder modulators operate with drive voltages that take values
in the discrete sets

$$\begin{aligned} V_1 &\in \{-V_{\pi_1}, V_{\pi_1}\} \\ V_2 &\in \{-V_{\pi_2}, V_{\pi_2}\} \end{aligned} \qquad (10.8)$$

The voltage of the phase shifter is set at $V_3 = V_{\pi_3}/2$, in order to introduce a
phase difference of $\pi/2$ between the two arms.

It is assumed that that the input into the QM is an unmodulated optical wave
whose complex envelope can be written as

$$\tilde{E}_{in}(t) = \sqrt{2P_s} e^{j\varphi_s} \qquad (10.9)$$

where P_s is the average optical power and ϕ_s is the initial phase of the transmitted
CW signal. In the previous formula, intensity and phase noises of the laser are
neglected. Then, the complex envelope of the output electric field can be written as

$$\tilde{E}_s(t) = \sqrt{P_s} e^{j\varphi_s + j\varphi_k} \qquad (10.10)$$

where $\varphi_k = \pm\pi/4, \pm 3\pi/4$.

10.3.2 Coherent Detection Fundamentals

The term *coherent* is used, in the context of optical communications, to refer to
any technique employing nonlinear mixing between two optical waves on a

semiconductor photodiode [4].[2] The carrier frequencies of the optical waves can be identical or different. In the former case, we have *coherent homodyne detection*. In the latter case, we have *coherent homodyne detection* (when the carrier frequency difference of the two waves is larger than or of the order of the symbol rate) or *coherent intradyne detection* (when the carrier frequency difference of the two waves is a fraction of the symbol rate).

The application of coherent homodyne detection for optical frequencies dates back to 1801, when Young proposed his now famous two-slit interference experiment as persuasive evidence of the wave nature of light [30]. In modern times, coherent heterodyne detection of electromagnetic waves has been used since the early days of radio communications. More specifically, heterodyne detection of radio waves was proposed by Fessenden [31], who also coined the term heterodyne from the Greek words 'heteros' (other) and 'dynamis' (force). Heterodyning gained immense popularity with the development of the superheterodyne receiver by E. H. Armstrong in 1921 [32]. Optical heterodyning was used for the first time by [33] in the visible part of the electromagnetic spectrum and by [34] in the infrared.

The earliest papers on coherent optical communication systems appeared in 1979, in Japanese, and in 1980, in English. The revived interest in coherent optical homodyne receivers in combination with advanced modulation formats started around 2004, e.g., see early articles [35–40].

10.3.2.1 Coherent Single-Ended Detection

The operating principle of coherent detection is explained in numerous textbooks, e.g., [41–42, 99]. Consider two traveling electromagnetic waves with carrier frequencies f_s and f_{lo}, respectively, from two independent laser sources, labeled the received signal and the local oscillator signal, respectively. The waves propagate in the same direction with identical states of polarization (SOP). Therefore, the electric fields of the two waves can be treated as scalars and they are denoted by $\vec{E}_s(t), \vec{E}_{lo}(t)$, respectively.

For simplicity, it is assumed that $E_s(t), E_{lo}(t)$ are both unmodulated (CW) sinusoidal signals

$$E_s(t) = \sqrt{2P_s} \cos(\omega_s t + \varphi_s)$$
$$E_{lo}(t) = \sqrt{2P_{lo}} \cos(\omega_{lo} t + \varphi_{lo})$$

(10.11)

---

[2] In contrast, in the digital communications literature the term *coherent* is used to refer to demodulation techniques in which the absolute phase of the incoming signal is tracked by the receiver. In optical communications, such receivers are called *synchronous*. In this report, we will be interested exclusively in coherent synchronous receivers.

where P_s, P_{lo} are the average optical powers, $\omega_s = 2\pi f_s, \omega_{lo} = 2\pi f_{lo}$ are the angular carrier frequencies, and φ_s, φ_{lo} are the initial phases of the received signal and the local oscillator signal, respectively. In the previous formulae, intensity and phase noises of the lasers are neglected.

The electric field of the combined signal impinging upon the photodiode, at a single detection point, can be written as the superposition of the electric fields of the received signal and the local oscillator

$$E_r(t) = E_s(t) + E_{lo}(t) \tag{10.12}$$

The photodiode is modeled as a square-law detector which responds to the square of the electric field

$$i(t) = R\left\langle E_s(t)^2 \right\rangle \tag{10.13}$$

where R is the responsivity of the photodiode and the angle brackets denote time averaging over an interval proportional to the response time of the photodiode.

By substituting Eqs. 10.12, 10.11 into Eq. 10.13 and using trigonometric identities, we obtain the following expression for the photocurrent in the absence of noise

$$i(t) = \underbrace{R[P_s + P_{lo}]}_{\substack{\text{direct}-\text{detection}\\\text{term}}} + \underbrace{2R\sqrt{P_s P_{lo}}\cos(\omega_{IF}t + \varphi_{IF})}_{\substack{\text{coherent}-\text{detection}\\\text{term}}} \tag{10.14}$$

where

$$\begin{aligned}\omega_{IF} &= 2\pi(f_s - f_{lo})\\ \varphi_{IF} &= \varphi_s - \varphi_{lo}\end{aligned} \tag{10.15}$$

It is observed that Eq. 10.14 is the sum of three terms due to the direct-detection of the received signal and the local oscillator signal, and their mixing (coherent detection term), respectively. The latter preserves the information transferred by the amplitude, the frequency and the phase of the received signal. Therefore, this type of detection can be used in conjunction with amplitude, frequency or phase modulation formats. In addition, the amplitude of the coherent detection term depends on the power of the local oscillator, which can be made very large. This is the reason for the improved receiver sensitivity exhibited by coherent detection.

10.3.2.2 Balanced Receiver

An implementation of the coherent receiver with fiber-optic components is shown in Fig. 10.6 [44, 118]. This configuration uses a directional 3-dB coupler and two identical p-i-n photodiodes connected back-to-back. A received signal of average power P_s and carrier frequency f_s is combined with the signal of a local oscillator of average power P_{lo} and carrier frequency f_{lo} on a directional 3-dB coupler. It is

Fig. 10.6 Balanced receiver
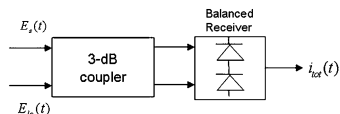
assumed that the states of polarization of the signal and the local oscillator are identical. The electric fields of the signal and the local oscillator are combined with ±90° relative phase shift at the two outputs of an ideal, lossless, polarization independent, directional 3-dB coupler. The output fields then illuminate the pair of two identical p-i-n photodiodes and produce two photocurrents. The outputs of the photodiodes are then subtracted, resulting in a combined photocurrent $i_{tot}(t)$. Since this receiver uses two photodiodes instead of one, it is called a *balanced receiver*. Balanced receivers are particularly attractive for use in optical coherent communication systems because they detect all received signal power, eliminate direct-detection terms and cancel excess intensity noise due to the local oscillator [44, 118].

For CW signal and local oscillator, the input electric fields are given by Eq. 10.11 and the final expression of the photocurrent, neglecting a $\pi/2$ phase constant, is given by (see Appendix B)

$$i_{tot}(t) = \underbrace{2R\sqrt{P_s P_{lo}}\cos(\omega_{IF}t + \varphi_{IF})}_{\text{coherent - detection term}} \qquad (10.16)$$

where R is the photodiode responsivity, ω_{IF} is the intermediate angular frequency defined as $\omega_{IF} = 2\pi(f_s - f_{lo})$ and $\varphi_{IF} = \varphi_s - \varphi_{lo}$.

10.3.2.3 Phase-Diversity Receiver

Phase-diversity receivers were initially proposed as a means of achieving homodyne detection with increased phase-noise tolerance, compared to homodyne detection with optical phase locking of the local oscillator [46]. They are based on multi-port couplers (called *optical hybrids*), which combine the signal and the local oscillator (LO) fields, introducing various phase shifts between the two, followed by multiple photodiodes to detect the combined optical signals. In the current context, phase-diversity receivers with 90° optical hybrids are used to separately recover the in-phase and quadrature components of the M-PSK signal downshifted in the baseband [47]. The phase noise is subsequently removed using a feed-forward phase estimation technique (see below).

Figure 10.7 shows an example of implementation of a phase-diversity receiver composed of a 4 × 4 90° optical hybrid and two balanced receivers (only the two-input ports are shown in the schematic). This configuration combines the best features of both phase-diversity and balanced receivers: it recovers the in-phase
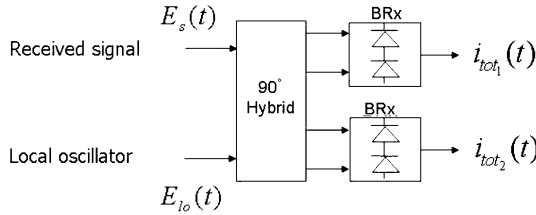
Fig. 10.7 Phase-diversity receiver using a 4×4 90° optical hybrid and two balanced receivers
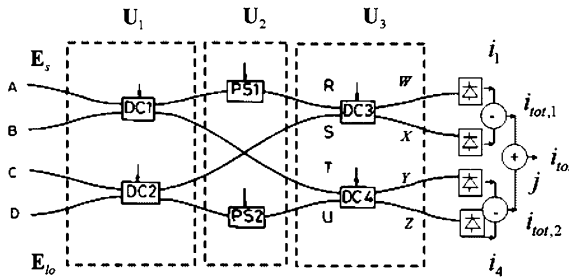

Fig. 10.8 Implementation of the 90° 4×4 hybrid. (Abbreviations: DC = direct current, PS = Phase shifter). (Symbols: $\mathbf{E}_s$=Received signal electric field vector, $\mathbf{E}_{lo}$=local oscillator electric field vector, $i_1 - i_4$: photocurrents at the four photodiodes, $i_{tot_{1,2}}$= phtocurrents at the output of the balanced receivers, i_{tot}=total complex photocurrent) (From [48], Fig. 10.2. Reproduced by permission of © 1989 The Institute of Electrical and Electronics Engineers.)

and quadrature components, while using all the available optical power of the received signal and the local oscillator, rejecting the direct-detection terms and the intensity noise of the local oscillator.

A hardware implementation of a 4×4 90° optical hybrid is shown in Fig. 10.8 and is analyzed in Appendix C [48]. A simpler but suboptimal implementation of a phase-diversity receiver proposed by [46, 117] uses a 2×2 90° optical hybrid (Fig. 10.9) and two matched photodiodes (not connected back-to-back, as in the case of a balanced receiver) and is analyzed in Appendix D.

As shown in Appendix C, for CW signal and local oscillator, the input electric fields are given by Eq. 10.11 and the final expression of the photocurrent, using the arrangement of Fig. 10.8, is given by

$$
\begin{aligned}
i_{tot_1}(t) &= \underbrace{R\sqrt{P_s P_{lo}}\cos(\omega_{IF}t + \varphi_{IF})}_{\text{in-phase component}} \\
i_{tot_1}(t) &= \underbrace{R\sqrt{P_s P_{lo}}\sin(\omega_{IF}t + \varphi_{IF})}_{\text{quadrature component}}
\end{aligned}
\tag{10.17}
$$

Fig. 10.9 Implementation of the 90° 2 × 2 hybrid. (Symbols: $\mathbf{E}_{1-8}$=Electric field vectors, $i_1 - i_2$: photocurrents at the two photodiodes)
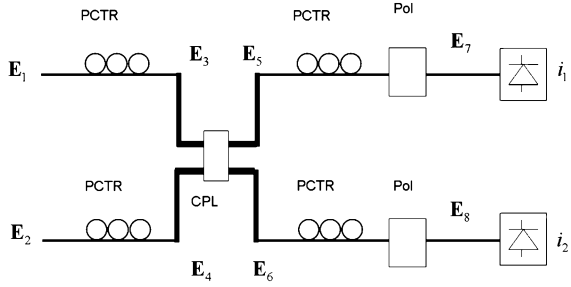
10.3.2.4 Polarization- and Phase-Diversity Receiver

So far, it was assumed that the SOPs of the signal and the local oscillator were identical. In reality, the SOP of the received signal is unknown and changes over time. In order to avoid outages, we use the polarization-diversity receiver configuration of Fig. 10.10. Using two polarization beam splitters (PBS), the signal and the local oscillator are analyzed in x, y linear polarizations, which are detected separately using two phase-diversity receivers.

As shown in Appendix E, for CW signal and local oscillator, the input electric fields are given by Eq. 10.11 and the final expression of the photocurrents in the upper branch are given by:

$$
\begin{aligned}
i_{tot_{1,x}}(t) &= \underbrace{R\sqrt{P_{s,x}P_{lo}/2}\cos(\omega_{IF}t + \varphi_{IF} + \varphi_x)}_{\text{in−phase component}} \\
i_{tot_{2,x}}(t) &= \underbrace{R\sqrt{P_{s,x}P_{lo}/2}\sin(\omega_{IF}t + \varphi_{IF} + \varphi_x)}_{\text{quadrature component}}
\end{aligned}
\tag{10.18}
$$

where $P_{s,x}$ is the power of the optical signal in the x-polarization and φ_x is a phase angle arising from the polarization mismatch between the signal and the local oscillator in the upper branch.

Similarly, the final expressions of the photocurrents in the lower branch are given by:

$$
\begin{aligned}
i_{tot_{1,y}}(t) &= \underbrace{R\sqrt{P_{s,y}P_{lo}/2}\cos(\omega_{IF}t + \varphi_{IF} + \varphi_y)}_{\text{in−phase component}} \\
i_{tot_{2,y}}(t) &= \underbrace{R\sqrt{P_{s,y}P_{lo}/2}\sin(\omega_{IF}t + \varphi_{IF} + \varphi_y)}_{\text{quadrature component}}
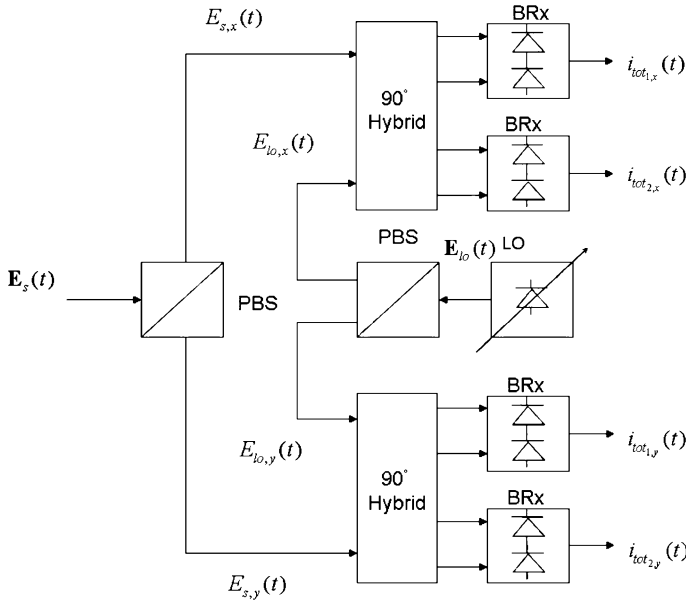\end{aligned}
\tag{10.19}
$$

Fig. 10.10 Implementation of the polarization-diversity receiver

where $P_{s,y}$ is the power of the optical signal in the x-polarization and φ_y is a phase angle arising from the polarization mismatch between the signal and the local oscillator in the lower branch.

By combining the photocurrents at the outputs of the balanced receivers in the upper branch of the polarization-diversity receiver with 90° phase shift we obtain

$$i_{tot_x}(t) = i_{tot_{1,x}}(t) + j i_{tot_{2,x}}(t) = R\sqrt{P_{s,x}P_{lo}/2}\,e^{j(\omega_{IF}t + \varphi_{IF} + \varphi_x)} \tag{10.20}$$

Similarly, by combining the photocurrents at the outputs of the balanced receivers in the lower branch of the polarization-diversity receiver with 90° phase shift, we obtain

$$i_{tot_y}(t) = i_{tot_{1,y}}(t) + j i_{tot_{2,y}}(t) = R\sqrt{P_{s,y}P_{lo}/2}\,e^{j(\omega_{IF}t + \varphi_{IF} + \varphi_y)} \tag{10.21}$$

Finally, the DSP unit samples the photocurrents with a sampling period T_s and forms the complex array

$$\mathbf{I}_{tot}(nT_s) = \begin{pmatrix} i_{tot,x} \\ i_{tot,y} \end{pmatrix} = R\sqrt{P_s P_{lo}/2}\,e^{j(\omega_{IF}nT_s + \varphi_{IF})}|e_s(nT_s)\rangle \tag{10.22}$$

where $|e_s(nT_s)\rangle$ is a normalized Jones vector which represents the received signal SOP at the instant nT_s.
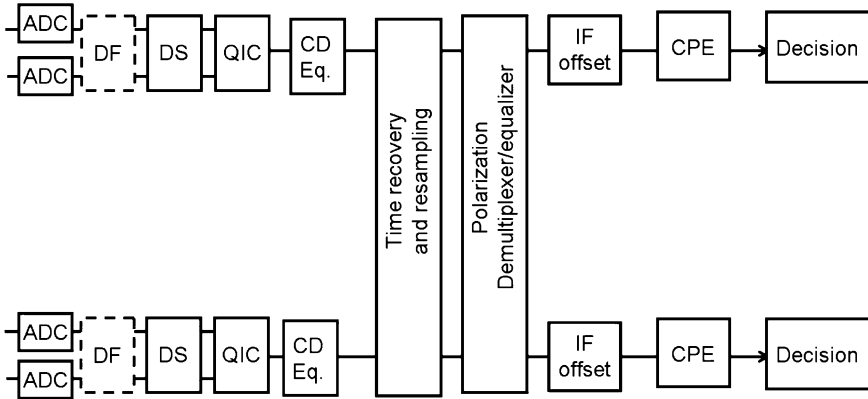
Fig. 10.11 DSP ASIC architecture (Symbols: ADC: analog-to-digital converter, DF: digital filter, QIC.: Quadrature imbalance estimation and compensation, CD eq.: fixed chromatic dispersion equalizer, IF offset: IF offset estimation and compensation, CPE: carrier phase estimation)

10.4 DSP Functionalities

In this section, we briefly review the DSP functionalities used in coherent optical intradyne PDM-QPSK receivers [50–53].

There is no unanimous agreement in the optical communications community regarding the optimal breakdown of DSP tasks, the order of the DSP modules, and the hardware implementation of different DSP algorithms. Figure 10.11 shows the most prominent view of the DSP ASIC's architecture [50–53].

Initially, the analog signals are converted to digital signals using analog-to-digital converters (ADCs) [54]. Conceptually, ADCs are composed of a sampler, which operates at a frequency that is not, in general, an integer multiple of the symbol rate, followed by a quantizer [26]. The amplitude of the signal samples at the output of the quantizer takes 2^k discrete values, where k denotes the number of ADC's resolution bits. Typically, state-of-the-art 56 GSa/s ADCs have 6–8 b resolution [54]. Current ADCs operate at a sampling frequency above the Nyquist rate, in order to achieve optimal performance, at the expense of hardware complexity and power consumption. For instance, employing two samples per symbol decreases timing errors and enables the use of robust fractionally spaced linear equalizers and digital timing recovery algorithms [51].

After the ADC, digital filtering (DF) might be performed in order to reject out-of-band signal frequency components and ASE noise [55]. The signal deskew (DS) module compensates for timing errors due to optical path length differences between the quadratures of each polarization tributary [56]. Then, quadrature imbalance, occurring at each phase-diversity receiver, is estimated and corrected (QIC). Quadrature imbalance is due to imperfections of the optical hybrid and

balanced receiver photodiode mismatch, which result in DC offsets, and both amplitude and phase errors in the output quadrature photocurrents [57–59]. Quadrature imbalance can be estimated by various techniques, e.g., by ellipse fitting of the constellation diagram [58, 60] or by computing the cross-correlation between the quadrature components of the received signal [61]. Quadrature imbalance compensation is typically achieved by Gram-Schmidt orthogonalization [58, 60, 61]. Other orthogonalization algorithms are proposed in [51]. A low implementation complexity feedback structure can be used in practice [53]. In principle, adaptive compensation of the quadrature imbalance, based on the constrained constant modulus algorithm (CMA), could also be used [69].

The two quadratures of each polarization tributary are then combined, via complex addition, to form discrete-time, scaled replicas of the received complex electric field vectors at the x- and y-polarizations, respectively.

Performance-wise, electronic chromatic dispersion post-compensation in coherent PDM-QPSK optical communications systems is superior to in-line optical compensation using dispersion compensating fibers (DCFs) [52]. Another advantage of electronic chromatic dispersion post-compensation over DCFs is that, in reconfigurable networks, the link length changes dynamically. The taps of electronic equalizers can be easily adjusted to accommodate for these changes [9]. In addition, in practice, the dispersion parameters of the optical fibers cannot be fully matched by DCFs, whereas the opposite is true for electronic equalizers [9]. Furthermore, the capital expenditure for implementing electronic equalization functionalities in the ASIC DSP chips can be relatively insignificant, when the latter are produced in large numbers. Finally, electronic equalization can compensate simultaneously for fiber nonlinearities by using back-propagation, e.g., based on the Manakov equation [62–68].

Electronic chromatic dispersion compensation is performed using a linear equalizer [50–53]. The transfer function of the linear equalizer is ideally the inverse transfer function of the optical fiber, the latter being modeled as a parabolic-phase, all-pass filter [42]. In practice, it can be implemented in time-domain by using a finite impulse response (FIR) filter with fixed coefficients [70, 71]. For large amounts of accumulated chromatic dispersion, a frequency domain implementation [76] is more computationally efficient than its time-domain counterpart [50, 52]. Several alternative approaches for reducing hardware complexity have been recently proposed (see [72–75, 50–53] and the references therein).

In experiments using real-time digital sampling oscilloscopes, the ADC sampling rate might not coincide with an integer multiple of the symbol rate. Therefore, the signals must be resampled to obtain an integer number of samples per bit. In a commercially available coherent receiver specifically designed for a specific symbol rate, such an operation might only be required for fine tuning. Signal resampling is a two-stage process that requires a clock-recovery scheme and an interpolation scheme. Typical non-data-aided digital clock-recovery algorithms from digital communications can be used [77] but their performance might be severely impaired, due to fiber transmission effects [78]. Several algorithms are specifically proposed for coherent optical intradyne PDM-QPSK receivers that are

robust to fiber transmission effects [79–82, 84]. Resampling can be achieved using either polynomial interpolation [27] or a fractional delay filter [85].

For polarization demultiplexing, as well as for removing signal distortion due to intersymbol interference arising from residual chromatic dispersion, polarization mode dispersion, polarization-dependent loss, and deterministic fiber nonlinearities, a blind adaptive two-input two-output (TITO) equalizer is used [50–53]. The equalizer attempts to counteract the channel effects by forming a linear superposition of the photocurrents. It is composed of four complex transversal filters with impulse responses w_{kl}, $k, l = 1, 2$, which are connected in a butterfly structure. For updating the filter coefficients, several variants of the constant modulus algorithm (CMA) [86, 87] can be used, possibly in conjunction with the decision-directed least-mean squares (DD-LMS) algorithm [87]. CMA-based blind adaptive equalizers are popular, due to their low computational complexity and their robustness in the presence of intermediate frequency (IF) offsets and laser phase noise. The second feature allows for decoupling between polarization demultiplexing and carrier frequency/phase recovery, so the latter two impairments can be addressed by separate DSP modules. A disadvantage of CMA-based modules is their possible erroneous convergence to the same PDM channel. The introduction of constraints on the CMA filter coefficients has been proposed for the correction of this defect, both for polarization demultiplexing only [88, 89], as well as for joint polarization demultiplexing/adaptive equalization [90, 91].

After polarization demultiplexing, the complex envelopes of the electric fields of the PDM-QPSK tributaries are recovered separately, at the upper and lower branches of the ASIC. The non-zero IF offset, due to the carrier frequency difference between the transmitter and the local oscillator lasers is estimated and removed. Several algorithms have been proposed for this purpose [92–95, 122].

A proliferation of algorithms has been proposed for carrier phase estimation (see for example [96, 97] and the references therein). The most commonly used is a feed-forward scheme initially proposed for burst digital transmission [123]. The algorithm can be modified to compensate for phase distortion due to interchannel cross-phase modulation as well [103, 124]. Its operating principle and its performance are explained in detail below.

10.4.1 Feed-Forward QPSK Carrier Phase Estimation Algorithm

The complex photocurrent at the input of the feed-forward carrier phase estimation module is proportional to the complex envelope of the received signal

$$x_k = A_k e^{j\phi_k} + n_{1_k} + j n_{2_k} \qquad (10.23)$$

where A_k is the instantaneous amplitude, φ_k is the instantaneous phase due to modulation, $\phi_k = \phi_s(kT_s) - \phi_{lo}(kT_s)$ is the total phase noise, and $n_{1,k} = n_1(kT_s), n_{2,k} = n_2(kT_s)$ are two independent additive Gaussian noises due to the combined action of ASE, shot and thermal noises.

The feed-forward phase-noise estimation algorithm uses N successive samples of x_k to produce an estimate of the average phase noise $\hat{\phi}$ during the N-symbol interval. To eliminate the phase modulation, the samples x_k are raised to the fourth power and added together. The receiver then uses the argument of the sum to estimate the phase noise, based on the expression

$$\hat{\phi} = \frac{1}{4}\arg\left(\sum_{k=1}^{N} x_k^4\right) \qquad (10.24)$$

Since the arg{.} function yields values in the interval $(-\pi, \pi)$, $\hat{\phi}$ is wrapped in the interval $(-\pi/4, \pi/4)$, whereas the actual phase noise is unbounded. Several phase unwrapping algorithms have been proposed in the optical communications literature, e.g., [96, 97]. Unsuccessful phase unwrapping can cause cycle slips [96, 97], which, in turn, can lead to catastrophic error bursts. Cycle slips can be mitigated by differential encoding and decoding (see below), at the expense of a slight increase of the bit error probability.

10.5 Other Receiver Functionalities

10.5.1 Gray Coding

At the M-PSK transmitter, an m-tuple of bits, where $m = \log_2 M$, is mapped into one of M distinct phase values. It is desirable to optimally associate the M phases with the binary m-tuples, in order to minimize the bit error probability. Since it is more likely that the noise added by the optical components will cause adjacent phase errors, mapping is performed using Gray coding [27, 83, 100–102], i.e., adjacent symbols in phase space differ only by one significant digit. With this code, an adjacent symbol error causes only one bit to be incorrect.

For illustration, Table 10.1(a)–(c) shows a two-, four-, and eight-level reflected Gray code [100]. It is observed that any two successive triplets in the list differ in exactly one position. The construction of the reflected Gray code is performed iteratively as follows: During the first iteration, $M = 2$, the Gray code set consists of the words 0 and 1 [Table 10.1(a)]. During the second iteration, $M = 4$, a set of new Gray code words is obtained by reflecting the set of words obtained during the first iteration about a horizontal line, then prefixing every element of the original set by zeros and its reflection by ones [Table 10.1(b)]. The same procedure is repeated during the third iteration, $M = 8$ [Table 10.1(c)], and so on.

Table 10.1 Two, four and eight-level Gray code (a), (b), (c)

Gray code word	Decimal no (n)	Phase change $\Delta\varphi_k = 2\pi_n/M$
(a)		
0	0	0
1	1	π
(b)		
00	0	0
01	1	$\pi/2$
11	2	π
10	3	$3\pi/2$
(c)		
000	0	0
001	1	$\pi/8$
011	2	$\pi/4$
010	3	$3\pi/8$
110	4	$\pi/2$
111	5	$5\pi/8$
101	6	$3\pi/4$
100	7	$7\pi/8$

10.5.2 Differential Coding

In coherent synchronous M-PSK receivers, there is a phase ambiguity due to the algorithm used in the phase-noise estimation [26, 29]. The phase ambiguity arises as follows: as described above, in order to estimate the carrier phase change due to phase noise, the received M-PSK signal is first raised to the M-th power to remove phase modulation. The argument of the resulting signal is divided by M to provide the carrier phase estimate. This process introduces a phase ambiguity of π/M. This is due to the fact that the M-PSK constellation is π/M rotation invariant. To eliminate this constant phase error due to the phase ambiguity, the information is encoded, not in absolute phases, but in the phase differences between two successive symbols. The resulting M-PSK signal is said to be differentially encoded (multilevel differentially encoded phase-shift keying, M-DEC-PSK).[3] A differential decoder is added at the output of the receiver in Fig. 10.3, in order to recover the original bit sequence. The decoder forms the differences between two successive symbols. Then, the constant phase error, due to the phase ambiguity in the carrier recovery, is eliminated.

---

[3] Without loss of generality, here we will adopt the term M-PSK instead of the more proper M-DEC-PSK.

Formally, we can mathematically describe the differential encoding process as follows:

At the transmitter, at the output of the mapper we obtain the complex symbols

$$c_k \equiv e^{j\Delta\varphi_k} \tag{10.25}$$

The differential encoder multiplies each consecutive symbol with the previously sent one. At the output of the differential encoder, we obtain the complex symbols with unit magnitude and argument equal to the sum between the present input and the previous total phase

$$d_k = e^{j\varphi_k} = d_{k-1}c_k = e^{j(\Delta\varphi_k + \varphi_{k-1})} \tag{10.26}$$

with initial condition $d_{-1} = e^{j\Phi}$, where Φ is a random initial phase.

At the output of the receiver, we recover the estimated differentially encoded symbols $\hat{d}_n$ which, in the ideal case, are equal to the transmitted ones d_n.

In order to form an estimate $\hat{c}_n$ of the original symbols c_n, the differential decoder uses the recursive function

$$\hat{c}_n = \hat{d}_n\hat{d}_{n-1}^* = e^{j(\Delta\varphi_n + \varphi_{n-1})}e^{-j\varphi_{n-1}} = e^{j\Delta\varphi_n} \tag{10.27}$$

where it is assumed that the initial value is $\hat{d}_{-1} = 1$.

10.6 Error Probability Evaluation

Error probability is the most appropriate design criterion for digital communications systems, since it is uniquely related to system capacity [26]. Different analytical expressions for the error probability of coherent optical QPSK systems in the presence of additive Gaussian noise and Gaussian phase noise, with various degrees of accuracy, are derived by different authors, e.g., [9, 36, 99, 104–106].

In the most rudimentary case, in the absence of intersymbol interference (ISI) and phase noise, in the exclusive presence of additive Gaussian noise, the bit error probability of a coherent optical QPSK system, assuming Gray coding, can be analytically calculated [26]

$$P_{e|b} = \frac{1}{2}\text{erfc}\left(\sqrt{\frac{\rho_s}{2}}\right) \tag{10.28}$$

where $\text{erfc}(z)$ is the complementary error function defined as [26]

$$\text{erfc}(z) = \frac{2}{\sqrt{\pi}}\int_z^\infty e^{-t^2}\,dt \tag{10.29}$$

In Eq. 10.28, ρ_s denotes the electronic SNR before the decision circuit, which is defined as [26]

$$\rho_s = \frac{A^2}{2\sigma^2} \tag{10.30}$$

where A is the amplitude of the complex envelope of the QPSK signal and σ^2 is the variance of each quadrature additive Gaussian noise component, due to the combined action of amplified spontaneous emission (ASE), shot and thermal noises.

If the additive Gaussian noise is exclusively due to amplified spontaneous emission (ASE) noise, the electronic symbol SNR is related to the optical signal-to-noise ratio (OSNR) by the expression (adapted from [20])

$$\text{OSNR} = \frac{pB_{eq}\rho_s}{2\Delta v_{res}}, \tag{10.31}$$

where $p = 1$ for single polarization channel transmission and $p = 2$ for PDM. In Eq. 10.31, Δv_{res} is the resolution bandwidth for the measurement of the ASE noise from the optical amplifiers and B_{eq} is the equivalent noise bandwidth [29] of the equivalent-baseband, aggregate transfer function of the transmission channel and the coherent optical receiver.

In the general case, in the presence of ISI, additive Gaussian noise, and Gaussian phase noise, we can use a computationally-efficient, semi-analytical method for the evaluation of the error probability of coherent optical PDM-QPSK systems.

According to the deterministic semi-analytical method [107], the distortion of the signal due to transmission impairments and the electronic DSP functionalities is computed by simulation in the absence of noise, the noise statistics at the input of the decision circuit are calculated analytically, and the average bit error probability is estimated using an analytical formula. More specifically, we evaluate the average symbol error probability using the arithmetic mean

$$\bar{P}_{e|s} = \frac{1}{N_{symbols}} \sum_{k=1}^{N_{symbols}} P_{e|s_k} \tag{10.32}$$

where $N_{symbols}$ denotes the number of simulated symbols and $P_{e|s_k}$ is the conditional error probability for the kth symbol.

We can transfer all constellation points to the upper right quadrant of the complex plane using appropriate rotations (i.e., multiples of $\pi/2$). Then, we can calculate the conditional error probability for the kth symbol by numerical integration using the formula (adapted from [36] with slight modifications)

$$P_{e|s_k} = \int_{-\infty}^{\infty} \text{erfc}\left[\sqrt{\rho_{s_k}}\cos(\theta_k + \varphi_k)\right]p_{\varphi_k}(\varphi_k)d\varphi_k$$

$$+ \int_{-\infty}^{\infty} \text{erfc}\left[\sqrt{\rho_{s_k}}\sin(\theta_k + \varphi_k)\right]p_{\varphi_k}(\varphi_k)d\varphi_k \qquad (10.33)$$

In Eq. 10.33, ρ_{s_k} is the instantaneous electronic symbol SNR before the decision circuit, defined as $\rho_{s|k} = A_k^2/(2\sigma^2)$ and $p_{\varphi_k}(\varphi_k)$ is the pdf of the residual phase noise, which is considered Gaussian to a first order approximation [97], with variance equal to (adapted from [106] with slight modifications, see Appendix F)

$$\sigma_{\varphi_k}^2 = Dt_k + \frac{DT}{3} - 2\frac{Dt_k}{T}\left(T - \frac{t_k}{2}\right) + \frac{\sigma^2}{2B_{eq}T} \qquad (10.34)$$

In Eq. 10.34, $D = 2\pi(\Delta v_s + \Delta v_{lo})$, where Δv_s, Δv_{lo} is the 3-dB spectral line-width of the lasers, T is the estimation (block) interval, t_k is the sampling time within the estimation interval, and B_{eq} is the equivalent-baseband, aggregate equivalent noise bandwidth of the coherent optical receiver. For a given system topology and assuming that the coherent homodyne receiver's adaptive filter coefficients are known, it is straightforward to analytically calculate the filtered additive Gaussian noise standard deviation σ, based on formulas from noise theory [26]. Finally, the average bit error probability, for Gray coding, is approximately $\bar{P}_{e|b} = 0.5\bar{P}_{e|s}$.

In order to take into account the ISI arising from m adjacent symbols on each side of the symbol we want to detect, we simulate all possible combinations of $2m + 1$ symbols [107]. Since each QPSK symbol takes four possible values, one needs to simulate, in principle, 4^{2m+1} quaternary symbols. This can be achieved by various methods [98, 107–109]. Here, we use two independent de Bruijn pseudo-random bit sequences, generated by different polynomials of periods equal to 2^{4m+3}, at the inputs of the QM.

In practice, the design of optical communications systems is based on the effective Q factor, which is related to the average bit error probability by the (arbitrary) equation [42]

$$\bar{P}_{e|b} = \frac{1}{2}\text{erfc}\left(\frac{\bar{Q}}{\sqrt{2}}\right) \qquad (10.35)$$

The corresponding effective Q factor is calculated by inverting (10.35)

$$\bar{Q} = \sqrt{2}\text{erfc}\left(2\bar{P}_{e|b}\right) \qquad (10.36)$$

10.7 Future Trends

Commercially available long-haul terrestrial coherent optical PDM-QPSK systems will be mostly used for transmitting 112 Gb/s per wavelength over 1500–2000 km of standard single-mode fiber (SSMF) and several reconfigurable optical add/drop multiplexers (ROADMs), using the current 50-GHz ITU WDM grid [12].

However, given the anticipated rate of future network traffic growth [110], the capacity of current long-haul terrestrial systems has to rapidly evolve to satisfy future bandwidth demands. Current research focuses on the development of coherent optical systems operating at 400 Gb/s or even 1 Tb/s per wavelength channel until 2020.

To achieve these data rates, a continuous increase in spectral efficiency is necessary, given the restrictions imposed by the ADC sampling rate and resolution, the required WDM channel spacing, and the optical amplifier bandwidth. In principle, higher spectral efficiencies can be achieved by using M-QAM, in single or multi-carrier coherent optical systems. However, as the size of the QAM constellation grows, there are severe limitations due to the increase in OSNR, the impact of nonlinearities, and the stringent requirements in laser linewidth imposed by laser phase noise. Winzer [12] explores the advantages and disadvantages of different alternative solutions.

Low-attenuation, large effective area optical fibers [111, 112], electronic compensation of fiber nonlinearities [62–68] and stronger forward error correction (FEC) codes [113], are some of the key enabling technologies that might influence the design of future coherent optical communications systems.

As a longer term solution for a drastic capacity increase, mode division multiplexing [114, 125] over few-mode fibers [115, 116] or multicore fibers [120] is also actively investigated.

Appendix A: Quadrature Modulator

In this Appendix, we derive a simplified mathematical model for the electro-optic QM in $LiNbO_3$.

In the subsequent analysis, the following notations are used [49]: Dirac's ket vectors denote Jones vectors, and boldface letters denote electric field vectors or scattering matrices (the distinction must be clear from context). In addition, analytic signals and complex envelopes are used (see definitions [26], Chap. 4) and are denoted by a hat and a tilde, respectively. These representations lead to elegant and concise mathematical expressions.

Using low pass equivalent formulation, the vector of the electric field of the transmitted optical signal can be written as

$$\mathbf{E}_s(t) = \Re\{\hat{\mathbf{E}}_s(t)\} \tag{10.37}$$

where $\Re\{\}$ denotes real part and $\hat{\mathbf{E}}_s(t)$ is the analytic electric field vector

$$\hat{\mathbf{E}}_s(t) = \tilde{\mathbf{E}}_s(t)e^{j\omega_s t} \tag{10.38}$$

In the above relationship, ω_s is the carrier angular frequency and $\tilde{\mathbf{E}}_s(t)$ is the complex envelope of the electric field

$$\tilde{\mathbf{E}}_s(t) = \tilde{E}_s(t)|e_s\rangle \tag{10.39}$$

where $|e_s\rangle$ is the normalized Jones vector that denotes the state of polarization (SOP) of the transmitted signal and $\tilde{E}_s(t)$ is the scalar complex envelope of the transmitted optical signal. For monochromatic electric fields, $\tilde{E}_s(t)$ corresponds to the electric field phasor.

As a starting point, we derive the transfer function of a Mach–Zehnder modulator, in terms of scattering matrices. A scattering matrix defines the relationship between the input and output analytic electric fields [119].

The scattering matrix of a lossless, polarization independent, directional 3-dB coupler is written [44, 45, 119]

$$\mathbf{S} = \frac{1}{\sqrt{2}}\begin{pmatrix} 1 & j \\ j & 1 \end{pmatrix} \tag{10.40}$$

The scattering matrix of the two parallel branches of a push–pull Mach–Zehnder modulator is written

$$\mathbf{D} = \begin{pmatrix} e^{\frac{j\phi}{2}} & 0 \\ 0 & e^{-\frac{j\phi}{2}} \end{pmatrix} \tag{10.41}$$

In the previous relationship, ϕ is the sum of a phase shift due to the propagation φ_0 and a phase shift due to the voltage-dependent refractive index (Pockels effect) [45]

$$\phi = \varphi_0 - \pi\frac{V}{V_\pi} \tag{10.42}$$

where

$$\begin{aligned} \varphi_0 &= \frac{2\pi}{\lambda_0}nL \\ V_\pi &= \frac{\lambda_0 d}{\mathfrak{r}n^3 L} \end{aligned} \tag{10.43}$$

where λ_0 is the free-space wavelength of the input optical beam, L is the length of the device, d is the distance between the electrodes, n is the effective refractive index in the absence of voltage, and $\mathfrak{r}$ is the Pockels electro-optic coefficient. The constant V_π is called half-wave voltage. The birefringence of LiNbO$_3$ is neglected.

The analytic electric fields at the output ports of the Mach–Zehnder modulator are

$$\begin{pmatrix} \hat{\mathbf{E}}_{o,1} \\ \hat{\mathbf{E}}_{o,2} \end{pmatrix} = \mathbf{SDS} \begin{pmatrix} \hat{\mathbf{E}}_{i,1} \\ 0 \end{pmatrix} = j \begin{pmatrix} \sin\frac{\phi}{2} \\ \cos\frac{\phi}{2} \end{pmatrix} \hat{\mathbf{E}}_{i,1} \tag{10.44}$$

where $\hat{\mathbf{E}}_{i,1}$ is the analytic electric field at one of the input ports of the Mach–Zehnder modulator.

Discarding the second output, the final result is

$$\hat{\mathbf{E}}_{o,1} = j\, \sin\frac{\phi}{2}\, \hat{\mathbf{E}}_{i,1} \tag{10.45}$$

For the analysis of the QM, we define the scattering matrices for the Mach–Zehnder modulators and the phase shifter as

$$\mathbf{M} = \begin{pmatrix} j\sin\frac{\phi_1}{2} & 0 \\ 0 & j\sin\frac{\phi_2}{2} \end{pmatrix}$$

$$\mathbf{\Phi} = \begin{pmatrix} e^{\frac{j\phi_3}{2}} & 0 \\ 0 & e^{-\frac{j\phi_3}{2}} \end{pmatrix} \tag{10.46}$$

The analytic electric fields at the output ports of the QM are

$$\begin{pmatrix} \hat{\mathbf{E}}_{o,1} \\ \hat{\mathbf{E}}_{o,2} \end{pmatrix} = \mathbf{S\Phi MS} \begin{pmatrix} \hat{\mathbf{E}}_{i,1} \\ 0 \end{pmatrix} \tag{10.47}$$

It is straightforward to show that, neglecting the phase shift due to the propagation φ_0,

$$\hat{\mathbf{E}}_{o,1} = \frac{j}{2} e^{-j\frac{\pi V_3}{2V_{\pi 3}}} \left\{ \sin\left[\frac{\pi V_1(t)}{2V_{\pi 1}}\right] - e^{-j\frac{\pi V_3}{2V_{\pi 3}}} \sin\left[\frac{\pi V_2(t)}{2V_{\pi 2}}\right] \right\} \hat{\mathbf{E}}_{i,1} \tag{10.48}$$

Since the polarizations are preserved we can write the following final relationship for the scalar complex envelopes

$$\tilde{E}_s(t) = \frac{j}{2} e^{-j\frac{\pi V_3}{2V_{\pi 3}}} \left\{ \sin\left[\frac{\pi V_1(t)}{2V_{\pi 1}}\right] - e^{-j\frac{\pi V_3}{2V_{\pi 3}}} \sin\left[\frac{\pi V_2(t)}{2V_{\pi 2}}\right] \right\} \tilde{E}_{in}(t) \tag{10.49}$$

Appendix B: Balanced Receiver

As discussed in Appendix A, the scattering matrix of a lossless, polarization independent, directional 3-dB coupler is written [45, 119]

$$\mathbf{S} = \frac{1}{\sqrt{2}} \begin{pmatrix} 1 & j \\ j & 1 \end{pmatrix} \tag{10.50}$$

The analytic electric fields at the output ports of the 3-dB coupler are

$$\begin{pmatrix} \hat{\mathbf{E}}_{o,1} \\ \hat{\mathbf{E}}_{o,2} \end{pmatrix} = \mathbf{S} \begin{pmatrix} \hat{\mathbf{E}}_s \\ \hat{\mathbf{E}}_{lo} \end{pmatrix} = \frac{1}{\sqrt{2}} \begin{pmatrix} \hat{\mathbf{E}}_s + j\hat{\mathbf{E}}_{lo} \\ j\hat{\mathbf{E}}_s + \hat{\mathbf{E}}_{lo} \end{pmatrix} \tag{10.51}$$

The photocurrent at the output of the two photodiodes is given by

$$i_k = \frac{R_k}{2} \hat{\mathbf{E}}_k^\dagger \hat{\mathbf{E}}_k \tag{10.52}$$

where R_k is the responsivity of the photodiodes and dagger denotes the adjoint matrix.

If the received analytic electric field $\hat{\mathbf{E}}_k$ is the sum of two analytic electric fields $\hat{\mathbf{E}}_k = \hat{\mathbf{E}}_{k,1} + \hat{\mathbf{E}}_{k,2}$, the photocurrent can be written

$$i_k = \frac{R_k}{2} \left[\hat{\mathbf{E}}_{k,1}^\dagger + \hat{\mathbf{E}}_{k,2}^\dagger \right] \left[\hat{\mathbf{E}}_{k,1} + \hat{\mathbf{E}}_{k,2} \right] = \frac{R_k}{2} \left\{ \left\| \hat{\mathbf{E}}_{k,1} \right\|^2 + \left\| \hat{\mathbf{E}}_{k,2} \right\|^2 + 2\Re \left[\hat{\mathbf{E}}_{k,2}^\dagger \hat{\mathbf{E}}_{k,1} \right] \right\} \tag{10.53}$$

By substitution of Eq. 10.51 into Eq. 10.53 we obtain

$$i_1 = \frac{R_1}{4} \left\{ \left\| \hat{\mathbf{E}}_s \right\|^2 + \left\| \hat{\mathbf{E}}_{lo} \right\|^2 + 2\Im \left[\hat{\mathbf{E}}_{lo}^\dagger \hat{\mathbf{E}}_s \right] \right\}$$
$$i_2 = \frac{R_2}{4} \left\{ \left\| \hat{\mathbf{E}}_s \right\|^2 + \left\| \hat{\mathbf{E}}_{lo} \right\|^2 - 2\Im \left[\hat{\mathbf{E}}_{lo}^\dagger \hat{\mathbf{E}}_s \right] \right\} \tag{10.54}$$

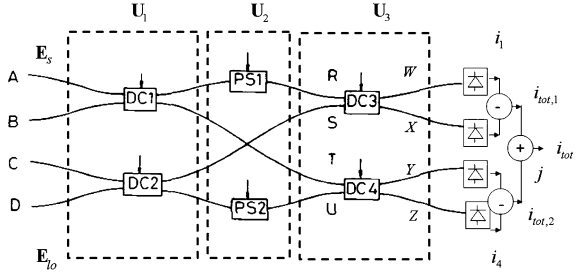where $\Im\{.\}$ denotes the imaginary part.

In the case $R_1 = R_2 = R$, we obtain

$$i_{tot} = i_1 - i_2 = R\Im \left[\hat{\mathbf{E}}_{lo}^\dagger \hat{\mathbf{E}}_s \right] \tag{10.55}$$

Appendix C: Analysis of a 4 × 4 90° Hybrid

The architecture of the four input/four output port optical hybrid is shown in Fig. 10.12 [48]. The received signal is fed into input A and split by an ideal,

Fig. 10.12 Implementation of the 90° 4 × 4 hybrid

lossless, polarization-independent 3-dB coupler (DC 1). The relative phase between the signals at the ports R and T can be tuned by a phase shifter (PS 1) to $2k\pi$. Similarly, the local oscillator signal is fed into input D and split by a second ideal, lossless, polarization-independent 3-dB coupler (DC 2). The phase between the local oscillator signal at the ports S and U is adjusted to 90° by a second phase shifter (PS 2). The split and phase shifted signals from the transmitter and the local oscillator are combined with four different phase shifts using two additional ideal, lossless, polarization-independent 3-dB couplers (DC 3, DC 4). The resulting optical signals at the output ports W, X, Y, and Z are detected by two balanced receivers. It will be shown that the total photocurrents at the output of the balanced receiversi_{tot_1}, i_{tot_2} correspond to coherent beating terms with a 90° phase difference between them.

The relationship that links the analytic electric fields at the input and output ports is:

$$\begin{pmatrix} \hat{\mathbf{E}}_W \\ \hat{\mathbf{E}}_X \\ \hat{\mathbf{E}}_Y \\ \hat{\mathbf{E}}_Z \end{pmatrix} = \mathbf{U}_3\mathbf{U}_2\mathbf{U}_1 \begin{pmatrix} \hat{\mathbf{E}}_A \\ \hat{\mathbf{E}}_B \\ \hat{\mathbf{E}}_C \\ \hat{\mathbf{E}}_D \end{pmatrix} = \mathbf{U}_3\mathbf{U}_2\mathbf{U}_1 \begin{pmatrix} \hat{\mathbf{E}}_s \\ 0 \\ 0 \\ \hat{\mathbf{E}}_{lo} \end{pmatrix} \qquad (10.56)$$

where $\hat{\mathbf{E}}_s, \hat{\mathbf{E}}_{lo}$ are the analytic electric fields of the signal and the local oscillator, respectively, omitting the time dependence to alleviate the formalism, and the matrices $\mathbf{U}_1, \mathbf{U}_2, \mathbf{U}_3$, that describe the transfer function of the respective broken rectangles in Fig. 10.12, are given by:

$$\mathbf{U}_1 = \mathbf{U}_3 = \frac{1}{\sqrt{2}} \begin{pmatrix} 1 & j & 0 & 0 \\ j & 1 & 0 & 0 \\ 0 & 0 & 1 & j \\ 0 & 0 & j & 1 \end{pmatrix} \qquad (10.57)$$

$$\mathbf{U}_2 = \begin{pmatrix} 1 & 0 & 0 & 0 \\ 0 & 0 & 1 & 0 \\ 0 & 1 & 0 & 0 \\ 0 & 0 & 0 & j \end{pmatrix} \qquad (10.58)$$

Performing the matrix multiplication in Eq. 10.56, it is straightforward to show that

$$
\begin{aligned}
\hat{\mathbf{E}}_W &= \frac{\hat{\mathbf{E}}_s - \hat{\mathbf{E}}_{lo}}{2} \\
\hat{\mathbf{E}}_X &= \frac{j}{2}\left(\hat{\mathbf{E}}_s + \hat{\mathbf{E}}_{lo}\right) \\
\hat{\mathbf{E}}_Y &= \frac{j}{2}\left(\hat{\mathbf{E}}_s + j\hat{\mathbf{E}}_{lo}\right) \\
\hat{\mathbf{E}}_Z &= \frac{j}{2}\left(j\hat{\mathbf{E}}_s + \hat{\mathbf{E}}_{lo}\right)
\end{aligned}
\tag{10.59}
$$

The photocurrent at the output of the four photodiodes is given by

$$
i_k = \frac{R_k}{2}\hat{\mathbf{E}}_k^\dagger \hat{\mathbf{E}}_k
\tag{10.60}
$$

where R is the responsivity of the photodiodes and dagger denotes the adjoint matrix.

If the received analytic electric field $\hat{\mathbf{E}}_k$ is the sum of two analytic electric fields $\hat{\mathbf{E}}_k = \hat{\mathbf{E}}_{k,1} + \hat{\mathbf{E}}_{k,2}$, the photocurrent can be written

$$
i_k = \frac{R_k}{2}\left[\hat{\mathbf{E}}_{k,1}^\dagger + \hat{\mathbf{E}}_{k,2}^\dagger\right]\left[\hat{\mathbf{E}}_{k,1} + \hat{\mathbf{E}}_{k,2}\right] = \frac{R_k}{2}\left\{\left\|\hat{\mathbf{E}}_{k,1}\right\|^2 + \left\|\hat{\mathbf{E}}_{k,2}\right\|^2 + 2\Re\left[\hat{\mathbf{E}}_{k,2}^\dagger \hat{\mathbf{E}}_{k,1}\right]\right\}
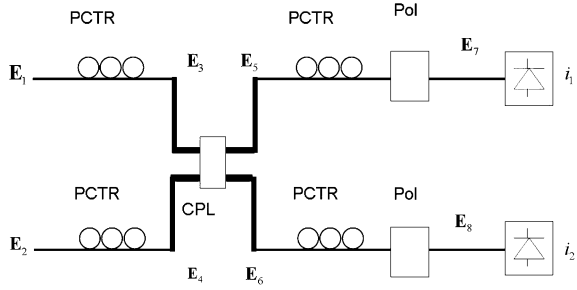\tag{10.61}
$$

where $\Re\{.\}$ denotes the real part.

By substitution of Eq. 10.59 into Eq. 10.61 we obtain

$$
\begin{aligned}
i_1 &= \frac{R_1}{8}\left\{\left\|\hat{\mathbf{E}}_s\right\|^2 + \left\|\hat{\mathbf{E}}_{lo}\right\|^2 - 2\Re\left[\hat{\mathbf{E}}_{lo}^\dagger \hat{\mathbf{E}}_s\right]\right\} \\
i_2 &= \frac{R_2}{8}\left\{\left\|\hat{\mathbf{E}}_s\right\|^2 + \left\|\hat{\mathbf{E}}_{lo}\right\|^2 + 2\Re\left[\hat{\mathbf{E}}_{lo}^\dagger \hat{\mathbf{E}}_s\right]\right\} \\
i_3 &= \frac{R_3}{8}\left\{\left\|\hat{\mathbf{E}}_s\right\|^2 + \left\|\hat{\mathbf{E}}_{lo}\right\|^2 + 2\Im\left[\hat{\mathbf{E}}_{lo}^\dagger \hat{\mathbf{E}}_s\right]\right\} \\
i_4 &= \frac{R_4}{8}\left\{\left\|\hat{\mathbf{E}}_s\right\|^2 + \left\|\hat{\mathbf{E}}_{lo}\right\|^2 - 2\Im\left[\hat{\mathbf{E}}_{lo}^\dagger \hat{\mathbf{E}}_s\right]\right\}
\end{aligned}
\tag{10.62}
$$

In the case $R_1 = R_2 = R_3 = R_4 = R$ we obtain

$$
\begin{aligned}
i_{tot,1} &= i_2 - i_1 = \frac{R}{2}\Re\left[\hat{\mathbf{E}}_{lo}^\dagger \hat{\mathbf{E}}_s\right] \\
i_{tot,2} &= i_3 - i_4 = \frac{R}{2}\Im\left[\hat{\mathbf{E}}_{lo}^\dagger \hat{\mathbf{E}}_s\right]
\end{aligned}
\tag{10.63}
$$

Fig. 10.13 Implementation of the 90° 2 × 2 hybrid

At the DSP we can form the complex photocurrent

$$i_{tot} = i_{tot,1} + ji_{tot,2} = \frac{R}{2}\hat{\mathbf{E}}_{lo}^{\dagger}\hat{\mathbf{E}}_s \tag{10.64}$$

Appendix D: Analysis of a 2 × 2 90° Hybrid

A 2 × 2 90° hybrid was proposed by [46, 117] (Fig. 10.13). The hybrid is composed of four polarization controllers (PCTR), an ideal, lossless, polarization-independent 3-dB coupler (CPL), and two fiber polarizers (Pol). The two-input polarization controllers change the state of polarization of the input signals to linear 45° and right-circular, respectively. The two-output polarization controllers change the principal axes of the fiber polarizers so that they select the $|x\rangle, |y\rangle$ polarization components of the optical signals at the output ports of the 3-dB coupler. The signals impingent to the photodiodes are proportional to $\hat{E}_1 + \hat{E}_2$ and $\hat{E}_1 + j\hat{E}_2$, respectively, where $\hat{E}_1, \hat{E}_2$ are the analytic signals corresponding to the input electric fields. The two-output photocurrents are calculated in this appendix and are shown to be in quadrature. In addition, it is shown that the detection of the two quadratures can be achieved by several different settings of the polarization controllers.

Simplified Model [46, 117]

After the two-input polarization controllers, the electric fields of the signal and the local oscillator can be written as

$$\hat{\mathbf{E}}_3(t) = \hat{E}_r(t)\frac{|x\rangle + |y\rangle}{\sqrt{2}} \tag{10.65}$$

$$\hat{\mathbf{E}}_4(t) = \hat{E}_{lo}(t) \frac{|x\rangle + j|y\rangle}{\sqrt{2}} \tag{10.66}$$

After the ideal, polarization-independent, lossless 3-dB coupler

$$\hat{\mathbf{E}}_5(t) = \frac{1}{\sqrt{2}} \left[\hat{\mathbf{E}}_3(t) + j\hat{\mathbf{E}}_4(t) \right] = \frac{1}{2} \left\{ \left[\hat{E}_r(t) + j\hat{E}_{lo}(t) \right] |x\rangle + \left[\hat{E}_r(t) - \hat{E}_{lo}(t) \right] |y\rangle \right\} \tag{10.67}$$

$$\hat{\mathbf{E}}_6(t) = \frac{1}{\sqrt{2}} \left[j\hat{\mathbf{E}}_3(t) + \hat{\mathbf{E}}_4(t) \right] = \frac{1}{2} \left\{ \left[j\hat{E}_r(t) + \hat{E}_{lo}(t) \right] |x\rangle + j\left[\hat{E}_r(t) + \hat{E}_{lo}(t) \right] |y\rangle \right\} \tag{10.68}$$

After the fiber polarizers

$$\hat{\mathbf{E}}_7(t) = \frac{1}{2} \left[\hat{E}_r(t) + j\hat{E}_{lo}(t) \right] |x\rangle \tag{10.69}$$

$$\hat{\mathbf{E}}_8(t) = \frac{j}{2} \left[\hat{E}_r(t) + \hat{E}_{lo}(t) \right] |y\rangle \tag{10.70}$$

At the photodiodes

$$
\begin{aligned}
i_1 &= \frac{R_1}{2} \hat{\mathbf{E}}_7^\dagger(t) \hat{\mathbf{E}}_7(t) = \frac{R_1}{8} \left| \hat{E}_r(t) + j\hat{E}_{lo}(t) \right|^2 \\
&= \frac{R_1}{8} \left\{ \left| \hat{E}_r(t) \right|^2 + \left| \hat{E}_{lo}(t) \right|^2 + 2\Im\left[\hat{E}_r(t)\hat{E}_{lo}^*(t) \right] \right\}
\end{aligned}
\tag{10.71}
$$

$$
\begin{aligned}
i_2 &= \frac{R_2}{2} \hat{\mathbf{E}}_8^\dagger(t) \hat{\mathbf{E}}_8(t) = \frac{R_2}{8} \left| \hat{E}_r(t) + \hat{E}_{lo}(t) \right|^2 \\
&= \frac{R_2}{8} \left\{ \left| \hat{E}_r(t) \right|^2 + \left| \hat{E}_{lo}(t) \right|^2 + 2\Re\left[\hat{E}_r(t)\hat{E}_{lo}^*(t) \right] \right\}
\end{aligned}
$$

Final expressions for laser offset and unmatched photodiodes

$$i_1 = \frac{R_1}{4} \left\{ P_r + P_{lo} + 2\sqrt{P_r P_{lo}} \sum_k g(t - kT) \sin[\omega_{IF} t + \phi_k + \theta(t)] \right\} \tag{10.72}$$

$$i_2 = \frac{R_2}{4} \left\{ P_r + P_{lo} + 2\sqrt{P_r P_{lo}} \sum_k g(t - kT) \cos[\omega_{IF} t + \phi_k + \theta(t)] \right\} \tag{10.73}$$

Generalized Model

The vector of the electric field of the received signal can be written as

$$\hat{\mathbf{E}}_1(t) = \hat{E}_r(t)\big|e'_r\big\rangle \tag{10.74}$$

The vector of the electric field of the local oscillator can be written as

$$\hat{\mathbf{E}}_2(t) = \hat{E}_{lo}(t)\big|e'_{lo}\big\rangle \tag{10.75}$$

After the polarization controllers

$$\hat{\mathbf{E}}_3(t) = \hat{E}_r(t)|e_r\rangle \tag{10.76}$$

$$\hat{\mathbf{E}}_4(t) = \hat{E}_{lo}(t)|e_{lo}\rangle \tag{10.77}$$

After the ideal, polarization-independent, lossless 3-dB coupler

$$\hat{\mathbf{E}}_5(t) = \frac{1}{\sqrt{2}}\left[\hat{\mathbf{E}}_3(t) + j\hat{\mathbf{E}}_4(t)\right] = \frac{1}{2}\left[\hat{E}_r(t)|e_r\rangle + j\hat{E}_{lo}(t)|e_{lo}\rangle\right] \tag{10.78}$$

$$\hat{\mathbf{E}}_6(t) = \frac{1}{\sqrt{2}}\left[j\hat{\mathbf{E}}_3(t) + \hat{\mathbf{E}}_4(t)\right] = \frac{1}{2}\left[j\hat{E}_r(t)|e_r\rangle + \hat{E}_{lo}(t)|e_{lo}\rangle\right] \tag{10.79}$$

After the fiber polarizers

$$\hat{\mathbf{E}}_7(t) = \frac{1}{2}\left[\hat{E}_r(t)\langle p_1 \mid e_r\rangle + j\hat{E}_{lo}(t)\langle p_1 \mid e_{lo}\rangle\right]|p_1\rangle \tag{10.80}$$

$$\hat{\mathbf{E}}_8(t) = \frac{1}{2}\left[j\hat{E}_r(t)\langle p_2 \mid e_r\rangle + \hat{E}_{lo}(t)\langle p_2 \mid e_{lo}\rangle\right]|p_2\rangle \tag{10.81}$$

We define

$$\begin{aligned}
\langle p_1 \mid e_r\rangle &= \alpha_1 e^{i\zeta_1} \\
\langle p_1 \mid e_{lo}\rangle &= \beta_1 e^{i\xi_1} \\
\langle p_2 \mid e_r\rangle &= \alpha_2 e^{i\zeta_2} \\
\langle p_2 \mid e_{lo}\rangle &= \beta_2 e^{i\xi_2}
\end{aligned} \tag{10.82}$$

At the photodiodes

$$i_1 = \frac{R_1}{2}\hat{\mathbf{E}}_7^{\dagger}(t)\hat{\mathbf{E}}_7(t) = \frac{R_1}{8}\left\{\alpha_1^2\big|\hat{E}_r(t)\big|^2 + \beta_1^2\big|\hat{E}_{lo}(t)\big|^2 + 2\alpha_1\beta_1\Im\left[\hat{E}_r(t)\hat{E}_{lo}^*(t)e^{i(\zeta_1-\xi_1)}\right]\right\} \tag{10.83}$$

$$i_2 = \frac{R_2}{2}\hat{\mathbf{E}}_8^{\dagger}(t)\hat{\mathbf{E}}_8(t) = \frac{R_2}{8}\left\{\alpha_2^2\big|\hat{E}_r(t)\big|^2 + \beta_2^2\big|\hat{E}_{lo}(t)\big|^2 - 2\alpha_2\beta_2\Im\left[\hat{E}_r(t)\hat{E}_{lo}^*(t)e^{i(\zeta_2-\xi_2)}\right]\right\}$$

Final expressions for laser offset and unmatched photodiodes

$$i_1 = \frac{R_1}{4}\left\{\alpha_1^2 P_r + \beta_1^2 P_{lo} + 2\alpha_1\beta_1\sqrt{P_r P_{lo}}\sum_k g(t-kT)\sin[\omega_{IF}t + \phi_k + \theta(t) + \zeta_1 - \xi_1]\right\}$$
$$(10.84)$$

$$i_2 = \frac{R_2}{4}\left\{\alpha_2^2 P_r + \beta_2^2 P_{lo} - 2\alpha_2\beta_2\sqrt{P_r P_{lo}}\sum_k g(t-kT)\sin[\omega_{IF}t + \phi_k + \theta(t) + \zeta_2 - \xi_2]\right\}$$
$$(10.85)$$

For ideal hybrid operation

$$(\zeta_2 - \xi_2) - (\zeta_1 - \xi_1) = (2k+1)\frac{\pi}{2} \tag{10.86}$$

Appendix E: Model of Polarization and Phase Diversity Receiver

In the upper branch, we receive

$$\hat{\mathbf{E}}_{s,x}(t) = \hat{E}_s(t)\langle x \mid e_s(t)\rangle|x\rangle$$
$$\hat{\mathbf{E}}_{lo,x}(t) = \frac{1}{\sqrt{2}}\hat{E}_{lo}(t)|x\rangle \tag{10.87}$$

In the lower branch, we receive

$$\hat{\mathbf{E}}_{s,y}(t) = \hat{E}_s(t)\langle y \mid e_s(t)\rangle|y\rangle$$
$$\hat{\mathbf{E}}_{lo,y}(t) = \frac{1}{\sqrt{2}}\hat{E}_{lo}(t)|y\rangle \tag{10.88}$$

The total photocurrent in the upper branch, in the absence of noise, is calculated by substituting Eq. 10.87 into Eq. 10.64

$$i_{tot,x} = \frac{R}{2\sqrt{2}}\hat{\mathbf{E}}_{lo}^\dagger\hat{\mathbf{E}}_{s,x} = \frac{R}{2\sqrt{2}}\hat{E}_{lo}^*\hat{E}_s\langle x \mid e_s(t)\rangle \tag{10.89}$$

Similarly, the total photocurrent in the lower branch, in the absence of noise, is calculated by substituting Eq. 10.88 into Eq. 10.64

$$i_{tot,y} = \frac{R}{2\sqrt{2}}\hat{\mathbf{E}}_{lo}^\dagger\hat{\mathbf{E}}_{s,y} = \frac{R}{2\sqrt{2}}\hat{E}_{lo}^*\hat{E}_s\langle y \mid e_s(t)\rangle \tag{10.90}$$

The DSP forms the following array, using the photocurrent of the two branches

$$\mathbf{I}_{tot} = \begin{pmatrix} i_{tot,x} \\ i_{tot,y} \end{pmatrix} = \frac{R}{2\sqrt{2}}\hat{E}_{lo}^*\hat{E}_s|e_s(t)\rangle \tag{10.91}$$

We observe that we are able to recover the full information content of the signal, regardless of the received signal SOP. However, there is a reduction in the photocurrent amplitude by $1/\sqrt{2}$.

Appendix F: Residual Phase-Noise Variance

The analytical calculation of the residual laser phase-noise variance, after the carrier phase estimation circuit proposed by [123], was done by [106]. In this Appendix, we rederive Eq. 10.34 from first principles, by approximating the phase-noise estimation averaging over discrete received signal samples as a continuous linear filtering process.

F.1 Laser Phase-Noise Properties

First, we review the basic properties of laser phase noise.

Phase noise is due to the spontaneous emission of semiconductor lasers. It can be modeled as a Wiener-Levy process, where the instantaneous phase is written as the integral of the random instantaneous angular frequency deviation $\dot{\phi}(t)$ [41]

$$\phi(t) = \int_0^t \dot{\phi}(t')dt' \tag{10.92}$$

The instantaneous angular frequency deviation $\dot{\phi}(t)$ can be interpreted as the difference between the instantaneous laser angular frequency $\omega_s(t)$ and the laser nominal angular carrier frequency ω_0, i.e.,

$$\dot{\phi}(t) = \omega_s(t) - \omega_0 \tag{10.93}$$

A common approximation is to assume that the instantaneous angular frequency deviation $\dot{\phi}(t)$ is just a zero-mean white Gaussian noise with psd

$$S_{\dot{\phi}}(\omega) = D \tag{10.94}$$

where D is a constant, which is called *phase diffusion coefficient*. It is linked to the 3-dB spectral linewidth of the laser. Since we are interested here for the total phase noise due to the transmitter laser and the local oscillator

$$D = 2\pi(\Delta\nu_s + \Delta\nu_{lo}), \tag{10.95}$$

where $\Delta\nu_s$, $\Delta\nu_{lo}$ is the 3-dB spectral linewidth of the lasers, respectively.

The autocorrelation function of the instantaneous angular frequency deviation is given by

$$R_{\dot{\phi}}(\tau) = \int\limits_{-\infty}^{\infty} S_{\dot{\phi}}(\omega)e^{j\omega\tau}df = D\int\limits_{-\infty}^{\infty} e^{j\omega\tau}df = D\delta(\tau) \qquad (10.96)$$

where $\delta(t)$ is the Dirac delta function.

From the above relationship, for $\tau = t_1 - t_2$

$$R_{\dot{\phi}}(t_1 - t_2) = E\left\{\dot{\phi}(t_1)\dot{\phi}(t_2)\right\} = D\delta(t_1 - t_2) \qquad (10.97)$$

The mean of the instantaneous angular frequency deviation is zero

$$\mu_{\dot{\phi}} = E\left\{\dot{\phi}(t)\right\} = 0 \qquad (10.98)$$

The variance of the instantaneous angular frequency deviation is given by

$$\sigma_{\dot{\phi}}^2 = R_{\dot{\phi}}(0) = D\delta(0) \qquad (10.99)$$

F.2   Mean and Variance of the Phase Noise

To determine the mean, we take the expected value of both sides of Eq. 10.92

$$\mu_{\phi} = E\{\phi(t)\} = \int\limits_{0}^{t} E\left\{\dot{\phi}(t')\right\}dt' = 0 \qquad (10.100)$$

To determine the variance, we use the definition

$$\sigma_{\phi}^2 = E\{\phi^2(t)\} = \int\limits_{0}^{t}\int\limits_{0}^{t} E\left\{\dot{\phi}(t_1)\dot{\phi}(t_2)\right\}dt_1 dt_2$$

$$= D\int\limits_{0}^{t}\int\limits_{0}^{t} \delta(t_1 - t_2)dt_1 dt_2 = D\int\limits_{0}^{t} dt_2 = Dt \qquad (10.101)$$

The cross-correlation function is

$$E\{\phi(t_1)\phi(t_2)\} = \int\limits_{0}^{t_1} \int\limits_{0}^{t_2} E\left\{\dot{\phi}(t_1')\dot{\phi}(t_2')\right\}dt_1'dt_2'$$

$$= D \int\limits_{0}^{t_1} \int\limits_{0}^{t_2} \delta\left(t_1' - t_2'\right)dt_1'dt_2' = D\min(t_1, t_2) \tag{10.102}$$

This agrees with the relationship Eq. 11.22 of [121], which is derived in a different manner.

F.3 Operation of the Feed-Forward Phase-Noise Estimation Circuit

The feed-forward phase-noise estimation circuit estimates the average of the received signal phase over a time interval T.

$$\bar{\phi} = \frac{1}{T} \int\limits_{0}^{T} \phi(t)dt \tag{10.103}$$

To determine the mean, we take the expected value of both sides of Eq. 10.92

$$\mu_{\bar{\phi}} = \frac{1}{T} \int\limits_{0}^{T} E\{\phi(t)\}dt = \mu_{\phi} = 0 \tag{10.104}$$

To determine the variance, we use the definition

$$\sigma_{\bar{\phi}}^2 = \frac{1}{T^2} \int\limits_{0}^{T} \int\limits_{0}^{T} E\{\phi(t_1)\phi(t_2)\}dt_1dt_2$$

$$= \frac{D}{T^2} \int\limits_{0}^{T} \int\limits_{0}^{T} \min(t_1, t_2)dt_1dt_2 \tag{10.105}$$

To evaluate the integral, we break it into a sum of two integrals, which correspond to the cases where $t_1 > t_2$ and $t_1 < t_2$

$$\sigma_{\bar{\phi}}^2 = \frac{D}{T^2} \left[\int\limits_0^T \left(\int\limits_0^{t_2} t_1 dt_1 \right) dt_2 + \int\limits_0^T \left(\int\limits_0^{t_1} t_2 dt_2 \right) dt_1 \right]$$

$$= \frac{D}{T^2} \int\limits_0^T t_2^2 dt_2 = \frac{DT}{3} \tag{10.106}$$

The averaging of the phasor of the unmodulated electric field corrupted by phase noise, in the case of an integrate and dump filter, i.e., an LPF whose impulse response is a rectangular pulse of duration T, was studied by [126]. In the realm of small phase noise, an analytical expression for the moment generating function of $\bar{\phi}$ is given by relation (6) in [126]. Double differentiation of (6) in [126] yields the same result like Eq. 10.105.

F.4 Operation of the Decision Circuit

The decision circuit makes a decision, which is corrupted by the remainder of phase noise

$$\theta(t) \cong \phi(t) - \bar{\phi} \tag{10.107}$$

To determine the mean, we take the expected value of both sides of Eq. 10.107

$$\mu_\theta = E\{\theta(t)\} = \mu_\phi - \mu_{\bar{\phi}} = 0 \tag{10.108}$$

To determine the variance, we use the definition

$$\sigma_\theta^2 = E\left\{ [\phi(t) - \bar{\phi}]^2 \right\} = E\{\phi^2(t) - 2\bar{\phi}\phi(t) + \bar{\phi}^2\}$$

$$= \sigma_\phi^2 + \sigma_{\bar{\phi}}^2 - 2E\{\bar{\phi}\phi(t)\} \tag{10.109}$$

The variances $\sigma_\phi^2, \sigma_{\bar{\phi}}^2$ are given by Eq. 10.101 and Eq. 10.105, respectively. We just have to evaluate the last term in Eq. 10.109.

$$E\{\bar{\phi}\phi(t)\} = \frac{1}{T} \int\limits_0^T E\{\phi(t)\phi(t_1)\} dt_1 = \frac{D}{T} \int\limits_0^T \min(t, t_1) dt_1 \tag{10.110}$$

Obviously, $0 \leq t \leq T$. As above, to evaluate the integral, we break it into a sum of two integrals which correspond to the cases $t_1 < t$ and $t_1 > t$

$$E\{\bar{\phi}\phi(t)\} = \frac{D}{T} \left(\int\limits_0^t t_1 dt_1 + t \int\limits_t^T dt_1 \right) = \frac{Dt}{T} \left(T - \frac{t}{2} \right) \tag{10.111}$$

In conclusion, the variance of the remainder of phase noise is given by

$$\sigma_\theta^2 = Dt + \frac{DT}{3} - 2\frac{Dt}{T}\left(T - \frac{t}{2}\right) \tag{10.112}$$

It is observed that the variance of the remainder of phase noise depends on the time instant in the time interval $[0, T]$. The maximum value occurs at the edges $t = 0$ and $t = T$ of the time interval and is equal to

$$\max\left(\sigma_\theta^2\right) = \frac{DT}{3} \tag{10.113}$$

The minimum value of error occurs in the middle $t = T/2$ of the time interval and is equal to

$$\min\left(\sigma_\theta^2\right) = \frac{DT}{12} \tag{10.114}$$

F.5   Receiver Photocurrent in the Presence of Additive Noise

For the $k-$th sample at the receiver, we define the auxiliary random variable

$$x_k = A_k e^{j\phi_k} + n_{1_k} + jn_{2_k} \tag{10.115}$$

where n_{1_k}, n_{2_k} are zero-mean white Gaussian processes with psd

$$S_{n_1}(f) = S_{n_2}(f) = \frac{N_0}{2} \tag{10.116}$$

Their autocorrelation functions are

$$R_{n_1}(t_1 - t_2) = R_{n_2}(t_1 - t_2) = \frac{N_0}{2}\delta(t_1 - t_2) \tag{10.117}$$

F.6   Small-Noise Approximation

Assuming negligible ISI, we set $A_k = A$. We factor out $Ae^{j\phi_k}$

$$x_k = A_k e^{j\phi_k}\left[\left(1 + n'_{1_k}\right) + jn'_{2_k}\right] \tag{10.118}$$

where we defined two new additive Gaussian noises n'_{1_k}, n'_{2_k} with zero mean and variance σ^2/A^2.

For small values of additive noise

$$x_k \cong Ae^{j\phi_k}\left(1 + jn'_{2_k}\right) = Ae^{j(\phi_k+\xi_k)} = Ae^{j\psi_k} \tag{10.119}$$

where we defined

$$\begin{aligned}
\psi_k &= \phi_k + \xi_k \\
\xi_k &= \tan^{-1} n'_{1_k} \cong n'_{2_k}
\end{aligned} \tag{10.120}$$

The new phase variable ξ_k has zero mean $\mu_\xi = 0$ and variance equal to

$$\sigma_\xi^2 = \sigma^2/A^2 \tag{10.121}$$

The new phase variable ψ_k has zero mean $\mu_\psi = 0$ and variance equal to

$$\sigma_\psi^2 = \sigma_\phi^2 + \sigma_\xi^2 \tag{10.122}$$

F.7 Operation of the Feed-Forward Phase-Noise Estimation Circuit

The feed-forward phase-noise estimation circuit estimates the average of the received signal phase over a time interval T.

$$\bar{\psi} = \frac{1}{T}\int_0^T \psi(t)dt = \frac{1}{T}\int_0^T [\phi(t) + \xi(t)]dt = \bar{\phi} + \bar{\xi} \tag{10.123}$$

To determine the mean, we take the expected value of both sides of Eq. 10.123

$$\mu_{\bar{\psi}} = \mu_{\bar{\phi}} + \mu_{\bar{\xi}} = 0 \tag{10.124}$$

To determine the variance, we use the property

$$\sigma_{\bar{\psi}}^2 = \sigma_{\bar{\phi}}^2 + \sigma_{\bar{\xi}}^2 \tag{10.125}$$

To determine the variance $\sigma_{\bar{\xi}}^2$, we use the definition

$$\begin{aligned}
\sigma_{\bar{\xi}}^2 &= \frac{1}{T^2}\int_0^T\int_0^T E\{\xi(t_1)\xi(t_2)\}dt_1dt_2 \\
&= \frac{N'_0}{2T^2}\int_0^T\int_0^T \delta(t_1 - t_2)dt_1dt_2 = \frac{N'_0}{2T} = N'_0 B_e
\end{aligned} \tag{10.126}$$

where we defined the equivalent electronic noise bandwidth as [29]

$$B_e = \frac{1}{2} \frac{\int\limits_{-\infty}^{\infty} |H_e(f)|^2 df}{|H_e(0)|^2} \qquad (10.127)$$

where $H_e(f)$ is the transfer function of the filter.

In our case, the feed-forward phase-noise estimation circuit can be thought of as an integrate and dump filter with impulse response

$$h_e(t) = \begin{cases} \frac{1}{T} & 0 \le t \le T \\ 0 & \text{elsewhere} \end{cases} \qquad (10.128)$$

Taking the inverse Fourier transform, we calculate the transfer function of the integrate and dump filter

$$H_e(f) = \int\limits_{-\infty}^{\infty} h_e(t) e^{-j\omega t} dt = \frac{\sin \pi f T}{\pi f T} e^{-j\omega T/2} \qquad (10.129)$$

From the above relationship, we notice that $|H_e(0)| = 1$ and using Parseval's theorem, we can analytically calculate the value of the equivalent electronic noise bandwidth

$$B_e = \frac{1}{2} \int\limits_{-\infty}^{\infty} |H_e(f)|^2 df = \frac{1}{2} \int\limits_{-\infty}^{\infty} h_e(t)^2 dt = \frac{1}{2T} \qquad (10.130)$$

It is worth noting that we do not take into account the correlation of the additive Gaussian noise samples due to the optical filter!

F.8 Operation of the Decision Circuit

The decision circuit makes a decision, which is corrupted by the remainder of phase noise and the additive white Gaussian noise

$$\varphi(t) = \phi(t) - \bar{\psi} = \theta(t) - \bar{\xi} \qquad (10.131)$$

To determine the mean, we take the expected value of both sides of Eq. 10.107

$$\mu_\varphi = E\{\varphi(t)\} = \mu_\theta - \mu_{\bar{\xi}} = 0 \qquad (10.132)$$

To determine the variance, we use the definition

$$\begin{aligned} \sigma_\varphi^2 &= E\left\{ \left[\theta(t) - \bar{\xi} \right]^2 \right\} = E\{ \theta^2(t) - 2\bar{\xi}\theta(t) + \bar{\xi}^2 \} \\ &= \sigma_\theta^2 + \sigma_{\bar{\xi}}^2 - 2E\{ \bar{\xi}\theta(t) \} \end{aligned} \qquad (10.133)$$

The final result is

$$\sigma^2_{\varphi_k} = Dt_k + \frac{DT}{3} - 2\frac{Dt_k}{T}\left(T - \frac{t_k}{2}\right) + \frac{\sigma^2}{2B_{eq}T} \qquad (10.134)$$

References

1. Sun H, Wu K-T, Roberts K (2008) Real-time measurements of a 40 Gb/s coherent system. Opt Exp 16(2):873–879
2. Roberts K, O'Sullivan M, Wu K-T, Sun H, Awadalla A, Krause DJ, Laperle C (2009) Performance of dual-polarization QPSK for optical transport systems. IEEE/OSA J Lightwave Technol 27(16):3546–3559
3. Okoshi T (1987) Recent advances in coherent optical fiber communication systems. IEEE/OSA J Lightwave Technol 5(1):44–52
4. Linke RA, Gnauck AH (1988) High-capacity coherent lightwave systems. IEEE/OSA J Lightwave Technol 6(11):1750–1769
5. Okoshi T, Kikuchi K (1988) Coherent optical fiber communications. Kluwer, Norwell
6. Betti S, de Marchis G, Iannone E (1995) Coherent optical communication systems. Wiley, New York
7. Ryu S (1995) Coherent lightwave communication systems. Artech House, Boston
8. Kikuchi K (2008) Coherent optical communication systems. In: Kaminow IP, Li T, Willner AE (eds.) Optical fiber telecommunications. vol VB, Academic, San Diego, CA, pp 95–129 (Chapter 3)
9. Ip E, Lau APT, Barros DFJ, Kahn JM (2008) Coherent detection in optical fiber systems. Opt Exp 16(2):753–791
10. Charlet G (2008) Coherent detection associated with digital signal processing for fiber optics communication. Comptes Rendus Physique 9(9–10):1012–1030
11. Li G (2009) Recent advances in coherent optical communication. Adv Opt Photon 1(2):279–307
12. Winzer P (2010) Beyond 100G Ethernet. IEEE Commun Mag 48(7):26–30
13. Kahn JM, Ho K-P (2004) Spectral efficiency limits and modulation/detection techniques for DWDM systems. IEEE J Select Topics Quant Electron 10(2):259–272
14. Winzer PJ, Essiambre R.-J (2008) Advanced optical modulation formats. In: Kaminow IP, Li T, Willner AE (eds.) Optical fiber telecommunications. vol. VB, Academic, San Diego, CA, pp 23–93 (Chapter 2)
15. Yu J, Zhou X (2009) Multilevel modulations and digital coherent detection. Opt Fiber Technol 15(3):197–208
16. Van den Borne D, Sleiffer V, Alfiad MS, Jansen SL, Wuth T (2009) POLMUX-QPSK modulation and coherent detection: The challenge of long-haul 100G transmission. In: Proceedings of European conference on optical communications (ECOC), paper 3.4.1, Vienna, Austria
17. Faure J.-P, Lavigne B, Bresson C, Bertran-Pardo O, Colomer AC, Canto R (2010) 40G and 100G deployment on 10G infrastructure: market overview and trends, coherent versus conventional technology. In: Proceedings of IEEE/OSA optical fiber communication conference (OFC/NFOEC), paper OThE3, San Diego, CA
18. Saunders R, Traverso M, Schmidt T, Malouin C (2010) Economics of 100 Gb/s transport. In: Proceedings of IEEE/OSA optical fiber communication conference (OFC/NFOEC), paper NMB2, San Diego, CA

19. Camera M (2010) 100GbE optical transport, appropriate modulation formats, and impact on deployed transport networks. In: Proceedings of IEEE/OSA optical fiber communication conference (OFC/NFOEC), paper NME3, San Diego, CA

20. Essiambre R-J, Kramer G, Winzer PJ, Foschini GJ, Goebel B (2010) Capacity limits of optical fiber networks. IEEE/OSA J Lightwave Technol 28(4):662–701

21. Ruhl F, Sorbello L, Evans D, Diaconescu L, Doucet D, Fasken D, Nimiczeck M, Sitch J, O'Sullivan M, Belanger M (2010) 2038 km and four 50 GHz OADM/filters transmission field trial of 115.2 Gb/s coherent CoFDM modem in the Telstra network. In: Proceedings of IEEE/OSA optical fiber communication conference (OFC/NFOEC), paper OThE3, San Diego, CA

22. Birk M, Gerard P, Curto R, Nelson LE, Zhou X, Magill P, Schmidt TJ, Malouin C, Zhang B, Ibragimov E, Khatana S, Glavanovic M, Lofland R, Marcoccia R, Saunders R, Nicholl G, Nowell M, Forghieri F (2010) Coherent 100 Gb/s PM-QPSK field trial. IEEE Commun Mag 48(7):52–60

23. Sano A, Masuda H, Kobayashi T, Fujiwara M, Horikoshi K, Yoshida E, Miyamoto Y, Matsui M, Mizoguchi M, Yamazaki H, Sakamaki Y, Ishii H (2010) 69.1-Tb/s (432 × 171-Gb/s) C- and extended L-band transmission over 240 km using PDM-16-QAM modulation and digital coherent detection. In: Proceedings of IEEE/OSA optical fiber communication conference (OFC/NFOEC), paper PDPB7, San Diego, CA

24. Zhou X, Yu J, Huang M.-F, Shao Y, Wang T, Nelson L, Magill P, Birk M, Borel PI, Peckham DW, Lingle R (2010) 64-Tb/s (640 × 107-Gb/s) PDM-36QAM transmission over 320 km using both pre- and post-transmission digital equalization. In: Proceedings of IEEE/OSA optical fiber communication conference (OFC/NFOEC), paper PDPB9, San Diego, CA

25. Nakazawa M, Okamoto S, Omiya T, Kasai K, Yoshida M (2010) 256 QAM (64 Gbit/s) coherent optical transmission over 160 km with an optical bandwidth of 5.4 GHz. In: Proceedings of IEEE/OSA optical fiber communication conference (OFC/NFOEC), paper OMJ5, San Diego, CA

26. Proakis J (2000) Digital communications, 4th edn. McGraw-Hill, New York, pp 177–178

27. Press WH, Teukolsky SA, Vetterling WT, Flannery BP (1992) Numerical recipes in C. Cambridge University Press, Cambridge, UK

28. Griffin RA, Carter AC (2002) Optical differentia1 quadrature phase-shift key (oQPSK) for high capacity optical transmission. In: Proceedings of IEEE/OSA optical fiber communication conference (OFC), paper WX6, Anaheim, CA

29. Benedetto S, Biglieri E, Castellani V (1987) Digital transmission theory. Prentice-Hall, Englewood Cliffs, NJ, pp 213–220

30. Serway R (1990) Physics for scientists and engineers. Saunders, Philadelphia

31. Fessenden RA (1902) Wireless signaling. U.S. Patent No. 706,740

32. Armstrong EH (1921) A new system of short wave amplification. Proc IRE 9(1):3–11

33. Forrester AT, Gudmundsen RA, Johnson PO (1961) Photoelectric mixing as a spectroscopic tool. J Opt Soc America 51(3):253–259

34. Teich MC, Keyes RJ, Kingston RH (1966) Optimum heterodyne detection at 10.6 pm in photoconductive Ge:Cu. Appl Phys Lett 9(10):357–360

35. Taylor MG (2004) Coherent detection method using DSP for demodulation of signal and subsequent equalization of propagation impairments. IEEE Photon Technol Lett 16(2):674–676

36. Noé R (2005) Phase noise tolerant synchronous QPSK/BPSK baseband-type intradyne receiver concept with feedforward carrier recovery. IEEE/OSA J Lightwave Technol 23(2):802–808

37. Noé R (2005) PLL-free synchronous QPSK polarization multiplex/diversity receiver concept with digital I&Q baseband processing. IEEE Photon Technol Lett 17(4):887–889

38. Ly-Gagnon D, Tsukamoto S, Katoh K, Kikuchi K (2006) Coherent detection of optical quadrature phase shift keying signals with carrier phase estimation. IEEE/OSA J Lightwave Technol 24(1):12–21

39. Kikuchi K (2006) Phase-diversity homodyne detection of multilevel optical modulation with digital carrier phase estimation. IEEE J Select Topics Quant Electron 12(4):563–570

40. Kazovsky LG, Kalogerakis G, Shaw WT (2006) Homodyne phase-shift-keying systems: past challenges and future opportunities. IEEE/OSA J Lightwave Technol 24(12):4876–4884

41. Kazovsky L, Benedetto S, Willner A (1996) Optical fiber communication system. Artech House, Boston, MA Chapter 4

42. Agrawal GP (2002) Fiber-optic communication systems, 3rd edn. Wiley, New York Chapter 10

43. Wenke G, Klimmek M (1996) Considerations on the α-factor of nonideal, external optical Mach–Zehnder modulators. J Opt Commun 17(2):42–48

44. Abbas GL, Chan VWS, Yee TK (1985) A dual-detector optical heterodyne receiver for local oscillator noise suppression. IEEE/OSA J Lightwave Technol 3(5):1110–1122

45. Saleh BEA, Teich MC (1991) Fundamentals of photonics. Wiley, New York Chapter 7

46. Kazovsky LG (1989) Phase- and polarization-diversity coherent optical techniques. IEEE/OSA J Lightwave Technol 7(2):279–292

47. Derr F (1992) Coherent optical QPSK intradyne system: concept and digital receiver realization. IEEE/OSA J Lightwave Technol 10(9):1290–1296

48. Hoffman D, Heidrich H, Wenke G, Langenhorst R, Dietrich E (1989) Integrated optics eight-port 90 hybrid on LiNbO$_3$. IEEE/OSA J LightwaveTechnol 7(5):794–798

49. Gordon JP, Kogelnik H (2000) PMD fundamentals: polarization mode dispersion in optical fibers. PNAS 97(9):4541–4550

50. Kuschnerov M, Hauske FN, Piyawanno K, Spinnler B, Alfiad MS, Napoli A, Lankl B (2009) DSP for coherent single-carrier receivers. IEEE/OSA J Lightwave Technol 27(16):3614–3622

51. Savory SJ (2010) Digital coherent optical receivers: algorithms and subsystems. IEEE J Select Topics Quant Electron 16(5):1164–1179

52. Spinnler B (2010) Equalizer design and complexity for digital coherent receivers. IEEE J Select Topics Quant Electron 16(5):1180–1192

53. Leven A, Kaneda N, Corteselli S (2010) Real-time implementation of digital signal processing for coherent optical digital communication systems. IEEE J Select Topics Quant Electron 16(5):1227–1234

54. Dedic I (2010) 56 GS/s ADC: Enabling 100GbE. In: Proceedings of IEEE/OSA optical fiber communication conference (OFC/NFOEC), paper OThT6, San Diego, CA

55. Winzer PJ, Gnauck AH, Doerr CR, Magarini M, Buhl LL (2010) Spectrally efficient long-haul optical networking using 112-Gb/s polarization-multiplexed 16-QAM. IEEE/OSA J Lightwave Technol 28(4):547–556

56. Tanimura T, Oda S, Tanaka T, Hoshida T, Tao Z, Rasmussen J (2009) A simple digital skew compensator for coherent receiver. In: Proceedings of European conference on optical communications (ECOC), paper 7.3.2, Vienna, Austria

57. Koc U, Leven A, Chen Y, Kaneda N (2006) Digital coherent quadrature phase-shift-keying (QPSK). In: Proceedings of IEEE/OSA optical fiber communication conference (OFC/NFOEC), paper OThI1, Anaheim, CA

58. Roudas I, Sauer M, Hurley J, MauroY, Raghavan S (2007) Compensation of coherent DQPSK receiver imperfections. In: Proceedings of IEEE LEOS summer topicals, paper MA3.4, Portland, OR

59. Petrou CS, Roudas I, Raptis L (2008) Impact of transmitter and receiver imperfections on the performance of coherent optical QPSK communication systems. In: Proceedings of the conference on lasers and electro-optics (CLEO), paper CThJJ1, San Jose, CA

60. Petrou CS, Vgenis A, Kiourti A, Roudas I, Hurley J, Sauer M, Downie J, Mauro Y, Raghavan S (2008) Impact of transmitter and receiver imperfections on the performance of coherent optical QPSK communication systems. In: Proceedings of IEEE/LEOS annual meeting, paper TuFF3, Newport Beach, CA

61. Fatadin I, Savory S, Ives D (2008) Compensation of quadrature imbalance in an optical QPSK coherent receiver. IEEE Photon Technol Lett 20(20):1733–1735

62. Ip E, Kahn JM (2008) Compensation of dispersion and nonlinear impairments using digital backpropagation. IEEE/OSA J Lightwave Technol 26(20):3416–3425

63. Mateo E, Li G (2009) Compensation of interchannel nonlinearities using enhanced coupled equations for digital backward propagation. Appl Opt 48(25):F6–F10

64. Goldfarb G, Li G (2009) Efficient backward-propagation using wavelet-based filtering for fiber backward-propagation. Opt Exp 17(11):8815–8821

65. Ip E, Kahn JM (2010) Fiber impairment compensation using coherent detection and digital signal processing. IEEE/OSA J Lightwave Technol 28(4):502–519

66. Ip E (2010) Nonlinear compensation using backpropagation for polarization-multiplexed transmission. IEEE/OSA J Lightwave Technol 28(6):939–951

67. Millar DS, Makovejs S, Behrens C, Hellerbrand S, Killey RI, Bayvel P, Savory SJ (2010) Mitigation of fiber nonlinearity using a digital coherent receiver. IEEE J Select Topics Quant Elec 16(5):1217–1226

68. Yaman F, Li G (2010) Nonlinear impairment compensation for polarization-division multiplexed WDM transmission using digital backward propagation. IEEE Photon J 2(5):816–832

69. Petrou CS, Vgenis A, Roudas I, Raptis L (2009) Quadrature imbalance compensation for PDM QPSK coherent optical systems. IEEE Photon Technol Lett 21(24):1876–1888

70. Savory SJ, Gavioli G, Killey RI, Bayvel P (2007) Electronic compensation of chromatic dispersion using a digital coherent receiver. Opt Exp 15(5):2120–2126

71. Savory SJ (2008) Digital filters for coherent optical receivers. Opt Exp 16(2):804–817

72. Goldfarb G, Li G (2007) Chromatic dispersion compensation using digital IIR filtering with coherent detection. IEEE Photon Technol Lett 19(13):969–971

73. Geyer, JC, Fludger CRS, Duthel T, Schulien C, Schmauss B (2010) Efficient frequency domain chromatic dispersion compensation in a coherent Polmux QPSK-receiver. In: Proceedings of IEEE/OSA optical fiber communication conference (OFC/NFOEC), paper OWV5, San Diego, CA

74. Geyer JC, Bisplinghoff A, Duthel T, Fludger CRS, Schulien C, Schmauss B (2010) Optimization of the chromatic dispersion equalizer of a 43 Gb/s realtime coherent receiver. In: Proceedings of IEEE/OSA optical fiber communication conference (OFC/NFOEC), paper OWV8, San Diego, CA

75. Khan FA, Agrell E, Karlsson M, (2010) Electronic dispersion compensation by Hadamard transformation. In: Proceedings of IEEE/OSA optical fiber communication conference (OFC/NFOEC), per OWV4, San Diego, CA

76. Kudo R, Kobayashi T, Ishihara K, Takatori Y, Sano A, Miyamoto Y (2009) Coherent optical single carrier transmission using overlap frequency domain equalization for long-haul optical systems. IEEE/OSA J Lightwave Technol 27(16):3721–3728

77. Meyr H, Moeneclaey M, Fechtel SA (1997) Digital communication receivers: synchronization, channel estimation, and signal processing. Wiley, New York

78. Zibar D, Bianciotto A, Wang Z, Napoli A, Spinnler B (2009) Analysis and dimensioning of fully digital clock recovery for 112 Gb/s coherent polmux QPSK systems. In: Proceedings of European conference on optical communications (ECOC), paper 7.3.4, Vienna, Austria

79. Fludger C, Duthel T, van den Borne D, Schulien C, Schmidt E-D, Wuth T, Geyer J, De Man E, Khoe G-D, de Waardt H (2008) Coherent equalization and POLMUX-RZ-DQPSK for robust 100-GE transmission. IEEE/OSA J Lightwave Technol 26(1):64–72

80. Kuschnerov M, Hauske FN, Gourdon E, Piyawanno K, Lankl B, Spinnler B (2008) Digital timing recovery for coherent fiber optic systems. In: Proceedings of IEEE/OSA optical fiber communication conference (OFC/NFOEC), paper JThA63, San Diego, CA

81. Tanimura T, Hoshida T, Oda S, Nakashima H, Yuki M, Tao Z, Liu L, Rasmussen JC (2008) Digital clock recovery algorithm for optical coherent receivers operating independent of laser frequency offset. In: Proceedings of European conference on optical communications (ECOC), Mo.3.D.2, Brussels, Belgium

82. Chang SH, Chung HS, Kim K (2008) Digital non-data-aided symbol synchronization in optical coherent intradyne reception. Opt Exp 16(19):15 097–15 103

83. Adachi F, Ohno K (1991) BER performance of QDPSK with postdetection diversity reception in mobile radio channels. IEEE Trans Vehic Technology 40(1):237–249

84. Louchet H, Kuzmin K, Richter A (2009) FFT-based digital clock recovery for coherent transmission systems with multilevel modulation formats. In: Proceedings of European conference on optical communications (ECOC), paper 7.3.5, Vienna, Austria

85. Laakso TI, Valimaki V, Karjalainen M, Laine UK (1996) Splitting the unit delay. IEEE Signal Process Mag 13(1):30–60

86. Godard D (1980) Self-recovering equalization and carrier tracking in two dimensional data communication systems. IEEE Trans Commun 28(11):1867–1875

87. Haykin S (1996) Adaptive filter theory, 3rd edn. Prentice Hall, Englewood Cliffs, NJ

88. Kikuchi K (2008) Polarization-demultiplexing algorithm in the digital coherent receiver. In: Proceedings of IEEE LEOS summer topicals, paper MC2.2, Acapulco, Mexico

89. Roudas I, Vgenis A, Petrou CS, Toumpakaris D, Hurley J, Sauer M, Downie J, Mauro Y, Raghavan S (2010) Optimal polarization demultiplexing for coherent optical communications systems. IEEE/OSA J Lightwave Technol 28(7):1121–1134

90. Vgenis A, Petrou CS, Papadias CB, Roudas I, Raptis L (2010) Nonsingular constant modulus equalizer for PDM-QPSK coherent optical receivers. IEEE Photonics Technol Lett 22(1):45–47

91. Xie C, Chandrasekhar S (2010) Two-stage constant modulus algorithm equalizer for singularity free operation and optical performance monitoring in optical coherent receiver. In: Proceedings of IEEE/OSA optical fiber communication conference (OFC/NFOEC), paper OMK3, San Diego, CA

92. Morelli M, Mengali U (1998) Feedforward frequency estimation for PSK: a tutorial review. European Trans Telecommun 2(2):103–116

93. Leven A, Kaneda N, Koc U-V, Chen Y-K (2007) Frequency estimation in intradyne reception. IEEE Photon Technol Lett 19(6):366–368

94. Li L, Tao Z, Oda S, Hoshida T, Rasmussen J (2008) Wide-range, accurate and simple digital frequency offset compensator for optical coherent receivers. In: Proceedings of IEEE/OSA optical fiber communication conference (OFC/NFOEC), paper OWT4, San Diego, CA

95. Hoffmann S, Bhandare S, Pfau T, Adamczyk O, Wördehoff C, Peveling R, Porrmann M, Noé R (2008) Frequency and phase-estimation for coherent QPSK transmission with unlocked DFB lasers. IEEE Photon Technol Lett 20(18):1569–1571

96. Ip E, Kahn J (2007) Feedforward carrier recovery for coherent optical communications. IEEE/OSA J LightwaveTechnol 25(9):2675–2692

97. Taylor MG (2009) Phase estimation methods for optical coherent detection using digital signal processing. IEEE/OSA J Lightwave Technol 27(7):901–914

98. Grellier E, Antona J.-C, Bigo S (2010) Are multilevel pseudorandom sequences really needed to emulate highly dispersive optical transmission systems?. In: Proceedings of European conference on optical communications (ECOC), paper We.6.A.1, Torino, Italy

99. Ho K-P (2005) Phase-modulated optical communication systems. Springer, New York

100. Lucky RW, Salz J, Weldon EJ (1968) Principles of data communication. McGraw-Hill, New York 13–15, 247–248

101. Weber WJ (1978) Differential encoding for multiple amplitude and phase shift keying systems. IEEE Trans Commun 26(3):385–391

102. Ma Y, Zhang QT (2002) Accurate evaluation for MDPSK with noncoherent diversity. IEEE Trans Commun 50(7):1189–1200

103. Tao Z, Li L, Liu L, Yan W, Nakashima H, Tanimura T, Oda S, Hoshida T, Rasmussen JC (2010) Improvements to digital carrier phase recovery algorithm for high-performance optical coherent receivers. IEEE J Select Topics Quant Electron 16(5):1201–1209

104. Bononi A, Bertolini M, Serena P, Bellotti G (2009) Cross-phase modulation induced by OOK channels on higher-rate DQPSK and coherent QPSK channels. IEEE/OSA J Lightwave Technol 27(18):3974–3983

105. Vanin E, Jacobsen G (2010) Analytical estimation of laser phase noise induced BER floor in coherent receiver with digital signal processing. Opt Exp 18(5):4246–4259

106. Goldfarb G, Li G (2006) BER estimation of QPSK homodyne detection with carrier phase estimation using digital signal processing. Opt Exp 14(18):8043–8053
107. Jeruchim M (1984) Techniques for estimating the bit error rate in the simulation of digital communication systems. IEEE J Select Areas Commun 2(1):153–170
108. van den Borne D, Gottwald E, Khoe GD, de Waardt H (2007) Bit pattern dependence in optical DQPSK modulation. Electron Lett 43(22):1223–1225
109. Spinnler B, Xie C (2007) Performance assessment of DQPSK using pseudo-random quaternary sequences. In: Proceedings of European conference on optical communications (ECOC), paper 2.3.6, Berlin, Germany
110. Tkach RW (2010) Scaling optical communications for the next decade and beyond. Bell Labs Tech J 14(4):3–10
111. Chen R, O'Sullivan M, Ward C, Asselin S, Belanger M (2010) Next generation transmission fiber for coherent systems. In: Proceedings of IEEE/OSA optical fiber communication conference (OFC/NFOEC), paper OTuI1, San Diego, CA
112. Charlet G (2010) Fiber characteristics for next-generation ultra-long-haul transmission systems. In: Proceedings of European conference on optical communications (ECOC), paper We.8.F.1, Torino, Italy
113. Smith BP, Kschischang FR (2010) Future prospects for FEC in fiber-optic communications. IEEE J Select Topics Quant Electron 16(5):1245–1257
114. Stuart HR (2000) Dispersive multiplexing in multimode optical fiber. Science 289(5477):281–283
115. Koebele C, Salsi M, Sperti D, Tran P, Brindel P, Mardoyan H, Bigo S, Boutin A, Verluise F, Sillard P, Astruc M, Provost L, Cerou F, Charlet G (2011) Two mode transmission at 2x100 Gb/s, over 40 km-long prototype few-mode fiber, using LCOS-based programmable mode multiplexer and demultiplexer. Opt Exp 19(17):16593–16600
116. Randel S, Ryf R, Sierra A, Winzer PJ, Gnauck AH, Bolle CA, EssiambreR-J, Peckham DW, McCurdy A, Lingle R (2011) 6×56-Gb/s mode-division multiplexed transmission over 33-km few-mode fiber enabled by 6×6 MIMO equalization. Opt Exp 19(17):16697–16707
117. Kazovsky LG, Curtis L, Young WC, Cheung NK (1987) An all fiber 90° optical hybrid for coherent communications. Appl Opt 26(3):437–439
118. Alexander SB (1987) Design of wide-band optical heterodyne balanced mixer receivers. IEEE/OSA J LightwaveTechnology 5(4):523–537
119. Green PE (1993) Fiber optic networks. Prentice Hall, Englewood Cliffs, NJ
120. Zhu B, Taunay TF, Fishteyn M, Liu X, Chandrasekhar S, Yan MF, Fini JM, Monberg EM, Dimarcello FV (2010) 112-Tb/s space-division multiplexed DWDM transmission with 14-b/s/Hz aggregate spectral efficiency over a 76.8-km seven-core fiber. Opt Exp 19(17):16665–16671
121. Papoulis A (1991) Probability, random variables, and stochastic processes, 3rd edn. McGraw-Hill, New York
122. Nakashima H, Tanimura T, Hoshida T, Oda S, Rasmussen J, Li L, Tao Z, Ishii Y, Shiota K, Sugitani K, Adachi H (2008) Novel wide-range frequency offset compensator demonstrated with real-time digital coherent receiver. In: Proceedings of European conference on optical communications (ECOC), paper Mo3.D.4, Brussels, Belgium
123. Viterbi A, Viterbi A (1983) Nonlinear estimation of PSK-modulated carrier phase with application to burst digital transmission. IEEE Trans on Inform Theory 29(4):543–551
124. Kuschnerov M, Chouayakh M, Piyawanno K, Spinnler B, de Man E, Kainzmaier P, Alfiad MS, Napoli A, Lankl B (2010) Data-aided versus blind single-carrier coherent receivers. IEEE Photon J 2(3):387–403
125. Shah AR, Hsu RCJ, Tarighat A, Sayed AH, Jalali B (2005) Coherent optical MIMO (COMIMO). IEEE/OSA J Lightwave Technol 23(8):2410–2419
126. Foschini GJ, Vannucci G (1998) Characterizing filtered light waves corrupted by phase noise. IEEE Trans Inform Theory 34(6):1437–1448